

2. EXPLANATORY NOTES¹

Shipboard Scientific Party²

INTRODUCTION

This chapter is designed to document the primary procedures and methods employed by the various shipboard laboratories in order to clarify the basis for our preliminary interpretations. This information pertains only to shipboard methods described in the site reports in the Leg 186 *Initial Reports* volume of the *Proceedings of the Ocean Drilling Program*. Methods for shore-based analysis of Leg 186 samples and data will be described in the individual scientific contributions to be published in scientific journals and in the *Scientific Results* volume.

Shipboard Scientific Procedures

Numbering of Sites, Holes, Cores, and Samples

Drilling sites are numbered consecutively from the first site drilled by the *Glomar Challenger* in 1968. At a site, multiple holes can be drilled by removing the drill pipe from the seafloor, moving the ship a short distance, and then drilling a new hole. For all Ocean Drilling Program (ODP) drill sites, a letter suffix distinguishes each hole drilled at the same site. The first hole drilled is assigned the site number modified by the suffix "A," the second hole is assigned the site number modified by the suffix "B," and so forth.

The cored interval is measured in meters below seafloor (mbsf). The depth below seafloor is determined by subtracting the water depth estimated from the initial drill-pipe measurement, which gives the length of pipe from the rig floor to the seafloor (measured in meters below rig floor [mbrf]), from the total drill-pipe measurement. Each cored interval is generally 9.5 m long, which is the length of a core barrel. Coring intervals may be shorter than 9.5 m and may not necessarily be adjacent if separated by drilled intervals.

¹Examples of how to reference the whole or part of this volume.

²Shipboard Scientific Party addresses.

A recovered core is divided into 1.5-m sections that are numbered serially from the top. When full recovery is obtained, the sections are numbered from 1 through 7, with the last section possibly being shorter than 1.5 m (Fig. F1); rarely, an unusually long core may require more than 7 sections. When less than full recovery is obtained, there will be as many sections as needed to accommodate the length of the core recovered. By convention, material recovered from the core catcher of a sedimentary core is placed in a separate section during the core description, labeled core catcher (CC), and placed below the last section recovered in the liner. The core catcher is placed at the top of the cored interval in cases where material is only recovered in the core catcher.

When the recovered core is shorter than the cored interval, the top of the core is equated with the top of the cored interval by convention to achieve consistency in handling analytical data derived from the cores. Samples removed from the cores are designated by distance measured in centimeters from the top of the section to the top and bottom of each sample removed from that section. A full identification number for a sample consists of the following information: leg, site, hole, core number, core type, section number, piece number (for hard rock), and interval in centimeters measured from the top of section. For example, a sample identification of “186-1150A-3H-5, 80–85 cm” would be interpreted as representing a sample removed from the interval between 80 and 85 cm below the top of Section 5, Core 3 (H designates that this core was taken during hydraulic piston coring) of Hole 1150A from Leg 186 (Fig. F1).

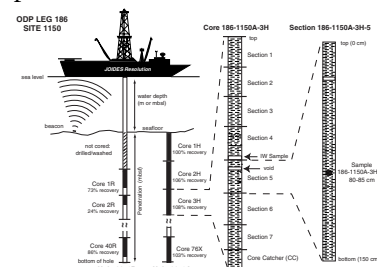
All ODP core identifiers indicate core type. The following abbreviations are used: H = hydraulic piston corer (also referred to as advanced hydraulic piston corer [APC]); X = extended core barrel (XCB); R = rotary core barrel (RCB); and M = miscellaneous material.

Core Handling

As soon as a core is retrieved on deck, it goes through a sequence of processing steps. First, a sample is taken from the core catcher and given to the paleontological laboratory for an initial age assessment. The core is then placed on a long horizontal rack. For safety monitoring, small (~5 cm³) plugs of sediment are taken from the end of one section per core for headspace gas analysis. Gas samples may also be taken by piercing the core liner, typically at voids, and withdrawing gas into a syringe. The core is then marked into section lengths, each section is labeled, and the core is cut into sections. Interstitial water (IW) whole-round samples are then taken as a matter of ODP policy (typically on every third core); whole-round samples for organic geochemistry may also be taken at this stage if they have been requested. For the cores that contain gas, several small holes are drilled into the core liners to allow gas to escape.

Each section is then sealed at the top and bottom by gluing on color-coded plastic caps. Blue caps identify the top of a section, and clear caps identify the bottom of a section. A yellow cap is placed on the section ends from which a whole-round sample has been removed, and the sample code (e.g., IW) is written on the yellow cap. The caps are usually attached to the liner by coating the end liner and the inside rim of the cap with acetone, and then the caps are taped to the liners. The core sections are then carried into the laboratory, where the individual sections are labeled with an engraver to permanently mark the full design-

F1. ODP sample labeling scheme, p. 35.



nation of the section. The length of the core in each section and the core-catcher sample are measured to the nearest centimeter; this information is logged into the ODP Janus database program.

Before they are split, whole-round core sections are run through the multisensor track (MST) and thermal conductivity measurements are taken. Whole-round samples for shore-based studies of consolidation, shear strength, and other elastic properties may be taken at this stage if they have been requested.

Cores of soft material are split lengthwise into working and archive halves. The softer cores are split with a wire or saw, depending on the degree of induration. Harder cores are split with a band saw or diamond saw. The cores are split from bottom to top, so investigators should be aware that older material could have been transported up the core on the split face of each section. Following the initial scientific measurements, both halves of the core are put into labeled plastic tubes, sealed, and transferred to cold-storage space aboard the drilling vessel. At the end of Leg 186, the cores were transferred from the ship in refrigerated containers to cold storage at the ODP Gulf Coast Repository in College Station, Texas.

LITHOSTRATIGRAPHY

The composition and texture of recovered sediments and sedimentary rocks were determined aboard ship by visual observation of the core and visual estimates of composition of particles in smear slides. X-ray diffraction (XRD) analyses were also used for identification of mineral assemblages. Color and digital images of sediments and sedimentary rocks were recorded by the spectrophotometer and digital camera to identify lithologic structure and quantitative color variation.

Core Descriptions

For each core we created an electronic core description sheet, which is a one-page graphic representation of the core lithology and other visual features, along with a text description (see the [“Core Descriptions”](#) contents list). The core description sheets were produced using the software package AppleCore (version 0.7.5g). Historically these have been referred to as “barrel sheets,” but here we use the term core description sheet. The information within these sheets is derived from smear-slide descriptions, handwritten descriptions, and hand-drawn graphics of each section, which were placed on “visual core description (VCD) sheets.” These handwritten notes are archived by ODP and are available upon request.

Each core description sheet includes a core identification label, which gives the site, hole, core number, and core type information following standard ODP nomenclature (see [“Introduction,”](#) p. 1). In addition, the cored interval is given in terms of the depth in mbsf. The body of the sheet includes a text description along with a graphic representation of lithology, drilling disturbance, bioturbation, structures, lithologic accessories, ichnofossils and fossils, samples, and fractures, along with a text description. The details of these are described below.

Graphic Representation

The lithology of the material recovered is represented on the core description sheet in the column titled “Graphic Lithology.” Sediment type is represented graphically using the patterns illustrated in Figure F2A. The major lithologies are divided into three main components: biogenic, siliciclastic, and volcanoclastic. The relative proportions of these shown in the Graphic Lithology column are based on smear-slide observations.

As many as three patterns, representing the three major components, may be used in the graphic lithology column. Constituents accounting for <10% of the sediment in a given lithology are not shown and are generally not included in the lithologic name. The graphic lithology column shows only the composition of layers or intervals exceeding 20 cm in thickness. Interbedded lithologies are represented as discrete layers divided by contacts as shown in Figure F2B.

Drilling Disturbance

Observations of drilling-related disturbance are recorded in the “Disturbance” column using the symbols shown in Figure F2B. The degree of drilling disturbance in soft and firm sediments is as follows:

1. Slight: bedding contacts are slightly deformed;
2. Moderate: bedding contacts have undergone significant bowing; and
3. Extreme: bedding is completely destroyed, and original structure cannot be recognized.

In addition to the degree of disturbance, the character of the disturbance is also described as follows:

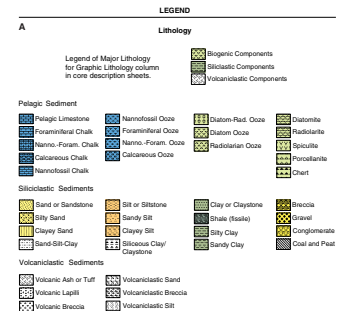
1. Disturbed: Bedding is generally intact, but sediment near the core liner is missing or homogenized;
2. Deformed: bedding contacts have been bent;
3. Soupy: Sediment is water saturated, and original structure is lost;
4. Flow-in: Sediment displays vertical structure caused by coring;
5. Slurry: Sediment homogenized during drilling;
6. Biscuit: pieces of partially indurated sediment in the core barrel; the pieces may represent contiguous stratigraphy with millimeter-sized cracks (slight) to small (<3 cm) pieces floating in slurry; and
7. Gas expansion: sediment voids, bubbles, or fractures in sediment caused by gas expansion.

Bioturbation

The apparent intensity of bioturbation is shown in the “Bioturbation” column of the barrel sheet in the conventional manner. The intensity of bioturbation is recognized on the basis of the following criteria (Fig. F2B):

1. Barren: sediments are undisturbed, whereas primary bedding and structures are fully obliterated by burrowing for “common” bioturbation;

F2. Leg 186 core description legend, p. 36.



2. Rare: primary depositional contacts are largely preserved but are cut by discrete burrows;
3. Moderate: fabric is dominated by biogenic structures, but primary depositional contacts are partially preserved; and
4. Common: biogenic fabric with no primary depositional contacts preserved.

Sedimentary and Deformational Structures

Natural structures and induced structures from the coring process can be difficult to distinguish in sediment cores. Natural structures observed are indicated in the “Structure” column of the core description form.

Sedimentary Structures

Sedimentary structures related to deposition and erosion, such as graded bedding, discrete trace fossils, soft-sediment deformation features, and diagenetic features, are illustrated in the structure column using the symbols shown in Figure F2B. Contacts (sharp, scoured, undulating, etc.) between lithologic beds, however, are illustrated in the graphic lithology column. Detailed features of these boundaries can be observed in the color image or photograph taken of each core. When scattered particles are sufficiently dense to form a discrete region but the boundaries are diffuse or unclear, the term “accumulation” is used. “Patch” means a circular or discrete region that has a different color or composition from the major lithology. Patches are commonly composed of clay, silt, or ash, and usually result from bioturbation.

Deformational Structures

The observed deformational structures interpreted to be of primary origin are graphically and descriptively represented on the VCD and core description sheets, using the symbols shown in Figure F2B. We describe the following visible characteristics: (1) the shape of the fracture (sharpness, straightness, and anastomosing or branching pattern); (2) apparent dip angle (measured with a conventional contact goniometer on the split surface of the archive-half core); (3) fracture infill thickness; (4) slickenside orientation; and (5) crosscutting relationships. The sense of relative displacement and amount of offset is noted where determinable.

A clear distinction was made between healed and open fractures because the moderate- to steep-dipping open fractures are interpreted to be drilling-induced ruptures of pre-existing healed fracture planes. These fractures are represented by the symbol for artificial fractures (this does not include the usual drilling fractures). The healed fractures are further divided into joints (without relative displacement of hanging to footwall blocks) and faults (with a finite value of displacement between hanging and footwall blocks). If the relative sense of movement could be determined, the symbols for normal and reverse faults are used. Evidence of displacement without apparent sense is termed a fault. Conjugate faults are also noted.

Ichnofossils and Fossils

The occurrence of ichnofossil genera and major groups of macro- and microfossils are assigned to the “Ichnofossils and Fossils” column. Symbols shown in this column are described in Figure F2C.

Lithologic Accessories

The positions of a variety of features are shown in the “Accessories” column. Symbols shown in this column are described in Figure F2D.

Samples

The positions of samples taken from each core for analysis are indicated by letters in the “Sample” column of the core description form as follows: SS (smear slide), WHC (whole-round core sample), PAL (micro-paleontology), and IW (interstitial water). Other samples collected for analysis during and after the cruise are listed in the Janus database.

Section Description

The text describing the lithology, found in the “Description” column of the core description sheet, consists of two parts: (1) a heading that lists all the major sediment lithologies observed in the core and (2) a general description of major and minor lithologies, including location of significant features in the core. Descriptions and locations of concretions; thin, interbedded lithologies; and other minor lithologies are included in the text, as is any clarifying information regarding sediment disturbance produced by drilling/coring or natural processes.

Smear Slides

Tables summarizing data from smear-slide analyses are provided (see the “Core Descriptions” contents list). These tables include information about the sample location, whether the sample represents a dominant (D) or a minor (M) lithology in the core, and the estimates of sand, silt, and clay proportions, together with all identified components.

Color and Diffuse Spectral Reflectance

Quantitative expression of sediment color was collected using the Minolta CM-2002 spectrophotometer on the archive multisensor track (AMST) for Site 1150 and using the scanner in handheld mode for Site 1151. The Minolta CM-2002 measures diffuse reflected visible light intensity in 31 bands ranging from 400 to 700 nm, with 10-nm resolution, and calculates and outputs data sets of $L^*a^*b^*$ value with XYZ and reflected intensity from 400 to 700 nm. Routine measurements were made every 2 cm for Site 1150 cores and every 5 cm for Site 1151. These measurements were determined on the archive split-core surface by covering each section with plastic wrap. The spectrophotometer was calibrated for white color reflectance and “zero calibrated” once or twice a day, typically at the beginning of each work shift.

The data collected for Site 1150 using the AMST has enhanced reflectance values, which result from an erroneous correction made by the AMST software. The software attempts to correct for the loss of reflectance that can happen when the scanner is not in direct contact with the core surface. In most cases, the true height offset is zero or very near zero; therefore, no correction should occur. The software, however, incorrectly estimates the height offset. It appears that a constant height-offset value has been hardwired into the software. The data appear to be useful, however, for determining where subtle color changes occur

downcore, but some caution is warranted. The data for Site 1151 are unaffected by the height-offset correction because all values were collected using the scanner in handheld mode with the scanner in contact with the core.

Digital Color Imaging

Digital color images of recovered core were taken for most cores from Site 1150 using a Kodak DSC460 digital camera with xenon flash lightings attached to the AMST. Each image covers a 10-cm interval. All images from a section are automatically combined into a single image and saved as a TIF image. Each image has a spacial resolution of 127 pixels/cm. Unfortunately, the two power supplies available for this unit failed and no digital images were taken of Site 1151 cores.

X-Ray Diffraction Measurements

Selected core samples were analyzed with an X-ray diffractometer (Philips PW 1729) to identify mineral assemblages and to estimate opal content and the composition of the terrigenous sedimentary fraction, semiquantitatively. Before analysis, bulk-sediment samples were freeze-dried and then ground. Step-scan measurements were run on random powder mounts with Cu radiation (40 kV and 35 mA) from 2° to 70° at steps of 0.02° θ per 2 s.

Graphic evaluation of the diffractograms was facilitated with the interactive MacDiff software (R. Petschick, public domain). Data were used for mineral identification on the basis of peak positions and relative intensities, as well as semiquantitative estimation of mineral abundances on the basis of both peak intensities and integrated peak areas.

Relative abundances of the minerals in the lithogenic fraction are presented only as relative changes in the peak height or peak areas of minerals. Diagnostic peaks of minerals found in the recovered sediments are listed in Table T1. Opal-A contents were estimated from the maximum peak height at 21.78° after subtracting the average height of background intensities extending between 16° and 39° in the X-ray diffractograms. In X-ray diffractograms of random powder mounts, most clay minerals yield a broad diffraction peak at ~4.5 Å. Smectite and mixed-layer clay minerals produce a very broad peak between 10 and 15 Å that is difficult to match precisely in the X-ray diffractograms. The integral peak areas centered at 14, 10, and 7 Å are only used for the estimation of relative clay mineral variations with depth. XRD data are compiled in a separate table in each site chapter. The halite peak at 2.82 Å results from crystallization of halite from interstitial water during drying of samples, and it is compiled for comparison with the salinity of interstitial water.

Classification of Sediments and Sedimentary Rocks

The major lithology of Leg 186 was predominantly mixed sediments, consisting of various admixtures of pelagic siliceous tests (mainly diatoms), silty clay and clay-sized siliciclastic grains, and volcanoclastic glass (ash). Pelagic calcareous grains were very rare. To increase clarification of the dominant component in the sediment, we modified Mazzullo et al. (1988) terminology (the standard ODP sediment classification scheme) to expand the designation of mixed sediments

T1. X-ray diffraction peaks used for mineral identification, p. 45.

that includes biogenic and siliciclastic components in the range between 40% and 60%.

We used the relative proportions of biogenic, siliciclastic, and volcanoclastic components to define the three major sediment classes (Fig. F3). Biogenic (pelagic) sediment is composed of >50% biogenic grains, siliciclastic sediments are composed of >50% siliciclastic grains, and volcanoclastic sediments are composed of >50% volcanoclastic grains. The definitions of biogenic, siliciclastic, and volcanoclastic particles are as follows:

1. Biogenic grains = skeletal debris produced in open-marine environments by (a) siliceous microfauna and microflora (radiolarians, diatoms, and associated organisms) and (b) calcareous microfauna and microflora (foraminifers, pteropods, nannofossils, and associated organisms);
2. Siliciclastic grains = grains comprising minerals and rock fragments that were eroded from plutonic, sedimentary, and metamorphic rocks; and
3. Volcanoclastic grains = grains comprising glass shards, rock fragments, and mineral crystals that were produced by volcanic processes.

Descriptive Terminology

Sediments and rocks were named on the basis of composition and texture using a principal name together with major and minor modifiers. Principal names define the degree of consolidation (induration) and granular sediment class as described above (Fig. F3).

Induration

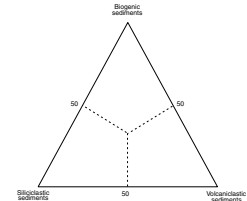
Induration of recovered sediments was defined using the modified terminology for calcareous sediments of Gealy et al. (1971). Three classes of induration were used to describe siliceous sediments and rocks during Leg 186. These classes are used as prefixes to sediment names.

1. Soft: sediments that have little strength and are readily deformed under the pressure of a fingernail or the broad blade of a spatula. Sediment core can be split with a wire cutter. This corresponds to the term “ooze” for pelagic sediments and pelagic clay or silt for siliciclastic sediments.
2. Firm: friable sediments that can be scratched with a fingernail or the edge of a spatula blade. It is difficult to split sediment cores with a wire cutter, but easy with the diamond saw.
3. Hard: nonfriable cemented rock, difficult or impossible to scratch with a fingernail or the edge of a spatula. The core is hard (i.e., consolidated or well indurated). It must be cut with a hand or diamond saw. For these materials, the suffix “-stone” is added to the soft-sediment name (e.g., sandstone, siltstone, and claystone).

Principal Names and Modifiers

The principal name refers to the component that comprises more than 50% of the lithology (Table T2). If no single component comprises more than 50%, the dominant component is given as the principal name. The principal name of biogenic, siliciclastic, or volcanoclastic

F3. Leg 186 sediment classification scheme, p. 39.



T2. Lithologic description of sediments and rocks, p. 46.

sediments is preceded by major modifiers and by minor modifiers, which have the suffix “-bearing.” Both major and minor modifiers refer to mixed biogenic, siliciclastic, or volcanoclastic components. The principal name (a) and modifiers (b and c) are used as follows, where the name of the sediment is given by c-bearing + b + a:

- a. Principal name: >50% or the dominant component when no single component is >50%;
- b. Major modifiers: 25%–50%;
- c. Minor modifiers: 10%–24%, given with the suffix “-bearing” (e.g., diatom-bearing); and
- d. Other modifiers: 3%–9%, components with these abundances are not named unless they are very important for interpretation.

For siliciclastic sediments, the principal name describes the texture and is assigned according to the following guidelines:

1. The Udden-Wentworth grain-size scale (Wentworth, 1922) defines the grain-size ranges and names of the textural groups (gravel, sand, silt, or clay) that are used as the principal names of siliciclastic sediment (Fig. F4).
2. When two or more textural groups are present in a siliciclastic sediment in sufficient amounts, they are listed as principal names in order of increasing abundance (Fig. F5).
3. The suffix “-stone” is affixed to the principal name sand, silt, and clay when the sediment is lithified (e.g., claystone).

The texture column in the smear-slide data tables (see the “**Core Descriptions**” contents list) shows the composition of texture, including all biogenic, siliciclastic, and volcanoclastic grains. The texture of siliciclastic sediment is given by relative proportion of texture only in siliciclastic grains.

Examples

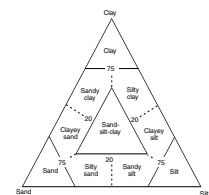
For a better understanding of the lithologic terminology, we give the following examples:

1. An unconsolidated sediment containing 40% biogenic (diatoms), 58% siliciclastic (clay), and 2% volcanic glass shards is termed “diatomaceous clay.”
2. An unconsolidated sediment containing 40% biogenic (diatoms), 58% siliciclastic (silty clay), and 2% volcanic glass shards is termed “diatomaceous silty clay.”
3. A hard, nonfriable cemented sediment containing 40% biogenic (diatoms), 58% siliciclastic (silty clay), and 2% volcanic glass shards is termed “diatomaceous silty claystone.”
4. An unconsolidated sediment containing 48% biogenic (diatoms), 45% siliciclastic (silty clay), 3% volcanic glass shards, and 5% other constituents is termed “silty clayey diatomaceous ooze.”
5. An unconsolidated sediment containing 60% biogenic (diatoms), 28% siliciclastic (silty clay), and 12% volcanic glass shards is termed “volcanic glass-bearing silty clayey diatomaceous ooze.”

F4. Udden-Wentworth grain-size classification of terrigenous sediments, p. 40.

Millimeters (mm)	Micrometers (µm)	Phi (φ)	Udden-Wentworth size class
4096	—	-12.0	Gravel
256	—	-8.0	
64	—	-6.0	
4	—	-2.0	
2.00	—	-1.0	Very coarse sand
1.00	—	0.0	
1.2	500	1.0	Sand
0.50	—	2.0	
0.14	250	3.0	
1.8	125	3.0	
1/16	0.0625	4.0	
1/32	0.031	5.0	
1/64	0.0156	6.0	Silt
1/128	0.0078	7.0	
1/256	0.0039	8.0	Clay
0.0006	0.06	14.0	

F5. Classification scheme used for siliciclastic sediments and rocks on Leg 186, p. 41.



6. An unconsolidated sediment containing 18% biogenic (diatoms), 52% siliciclastic (silty clay), and 30% volcanic glass shards is termed “diatom-bearing volcanic glassy silty clay.”
7. An unconsolidated sediment containing 35% biogenic (diatoms), 20% siliciclastic (silty clay), and 45% volcanic glass shards is termed “silty clay-bearing diatomaceous volcanic ash.”
8. An unconsolidated sediment containing 8% biogenic (diatoms), 90% siliciclastic (silty clay), and 2% volcanic glass shards is termed “silty clay.”
9. An unconsolidated sediment containing 38% biogenic (diatoms), 2% siliciclastic (silty clay), and 60% volcanic glass shards is termed “diatomaceous volcanic ash.”
10. An unconsolidated sediment containing 8% biogenic (diatoms), 2% siliciclastic (silty clay), and 90% volcanic glass is termed “volcanic ash.”

BIOSTRATIGRAPHY

Time Scale/Chronological Framework

During Leg 186, diatoms and calcareous nannofossils were studied to assess biostratigraphic constraints on the sedimentary sections at Sites 1150 and 1151. Age assignments were primarily made on core-catcher samples. However, additional samples from within the core were studied when a core-catcher sample was found to be inconclusive or otherwise unrepresentative of the core in its entirety.

Diatom datums of the North Pacific have been calibrated to Cande and Kent’s (1995) geomagnetic polarity time scale ([GPTS] CK95) by Motoyama and Maruyama (1998) and Yanagisawa and Akiba (1998). All age estimates of nannofossil datums are based on the time scale of Berggren et al. (1995), which incorporates the GPTS of CK95. The diatom and nannofossil zones are correlated to each other and to the GPTS of CK95, as shown in Figure F6.

Biostratigraphy

Diatoms

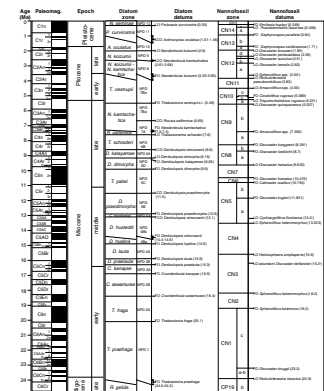
Zonation

The diatom zonation (Fig. F6) used for the Neogene follows the zonation of Motoyama and Maruyama (1998). This zonation is based on Koizumi and Tanimura (1985) and Koizumi (1985) for the datums above the *Neodenticula kamtschatica* Zone (7.3–7.4 to 6.65 Ma) and on Barron and Gladenkov (1995) for the lower datums down to the *Thalassiosira fraga* Zone (20.1–18.4 Ma). The earliest Miocene *Thalassiosira praeфрага* Zone (24.0–24.3 to 20.1 Ma) is defined based on Yanagisawa and Akiba (1998). Code numbers of North Pacific diatom zones by Yanagisawa and Akiba (1998) were adapted to the zonation.

Datum Levels

Table T3 lists age estimates for the Neogene diatom datum levels that have been found to be useful in the middle to high latitudes of the North Pacific represented by Motoyama and Maruyama (1998), except for the first occurrence of *T. praeфрага* (24.0–24.3 Ma) calibrated to CK95 by Yanagisawa and Akiba (1998). These ages are originally based on Bar-

F6. Correlation of the Neogene chronostratigraphy, biostratigraphy, and magnetostratigraphy used during Leg 186, p. 42.



T3. Estimated ages of diatom events used during Leg 186, p. 47.

ron (1980, 1992), Koizumi and Tanimura (1985), Akiba (1986), Gersonde and Burckle (1990), Baldauf and Barron (1991), Koizumi (1992), and Barron and Gladenkov (1995).

Methods

Smear slides were routinely examined for stratigraphic markers. When required (because of low concentration of specimens), selected samples were processed by boiling them in hydrogen peroxide and hydrochloric acid, followed by centrifuging at 1200 rpm for 2–4 min to remove the chemical solutions from the suspension.

These slides were examined in their entirety at a magnification of 500× for stratigraphic markers and paleoenvironmentally sensitive taxa. Identifications were checked routinely at 1250×. These abundances were recorded as follows:

- D (dominant) = more than five specimens per field of view,
- A (abundant) = two or more specimens per field of view,
- C (common) = one specimen per two fields of view,
- F (few) = one specimen per each vertical traverse,
- R (rare) = one specimen per a few traverses,
- T (trace) = one specimen per several or more vertical traverses, and
- B (barren).

Preservation of diatoms was qualitatively determined as follows:

- VG (very good) = finely silicified forms present, with no alteration of frustules, and some colonies of frustules preserved;
- G (good) = finely silicified forms present and no alteration of frustules observed;
- M (moderate) = finely silicified forms present with some alteration; and
- P (poor) = finely silicified forms absent or rare and fragmented, and the assemblage is dominated by robust forms.

Calcareous Nannofossils

The zonal schemes of Martini (1971; with modifications by Martini and Muller, 1986) and Bukry (1973, 1975; zonal code numbers added and modified by Okada and Bukry, 1980) were used for Cenozoic calcareous nannofossils (Fig. F6; Table T4).

Methods

Standard smear slides were made of all soft lithologies. Calcareous nannofossils were examined using standard light microscope techniques, under cross polarizers, transmitted light, and phase contrast at 1000× magnification.

Preservation and abundance of calcareous nannofossil species may vary significantly because of etching, dissolution, or calcite overgrowth. A simple code system to characterize preservation has been adopted and is listed below:

- VG = very good preservation (no evidence of dissolution and/or overgrowth; no alteration of primary morphological characteristics, and specimens appear diaphanous; specimens are identifiable to the species level);

T4. Estimated ages of calcareous nannofossil events used during Leg 186, p. 48.

- G = good preservation (little or no evidence of dissolution and/or overgrowth; primary morphological characteristics only slightly altered; specimens are identifiable to the species level);
- M = moderate preservation (specimens exhibit some etching and/or overgrowth; primary morphological characteristics somewhat altered; however, most specimens are identifiable to the species level); and
- P = poor preservation (specimens are severely etched or exhibit overgrowth; primary morphological characteristics largely destroyed; fragmentation has occurred; specimens cannot be identified at the species and/or generic level.

Six calcareous nannofossil abundance levels are recorded as follows:

- V = very abundant (10–100 specimens per field of view);
- A = abundant (1–10 specimens per field of view);
- C = common (1 specimen per 2–10 fields of view);
- F = few (1 specimen per 11–100 fields of view);
- R = rare (1 specimen per 101–1000 fields of view); and
- B = barren.

PALEOMAGNETISM

Paleomagnetic studies conducted on the *JOIDES Resolution* during Leg 186 consisted of remanent magnetization measurements of archive-half sections and discrete samples from the working-half sections. Measurements were made before and after alternating field (AF) demagnetization. To investigate rock magnetic properties, we measured the anisotropy of magnetic susceptibility and conducted thermal demagnetization, anhysteretic remanent magnetization (ARM), and isothermal remanent magnetization (IRM) experiments on some of the discrete samples. Magnetic susceptibility was also measured on whole-core sections using the MST device.

Instruments and Measurements

Measurements of remanent magnetization were conducted using an automated pass-through cryogenic magnetometer with a direct-current superconducting quantum interference device (2-G Enterprises Model 760-R), which has an in-line AF demagnetizer (2-G Enterprises Model 2G600) capable of producing peak fields of 80 mT with a 200-Hz frequency. Based on tests conducted during Leg 186, the background noise level of the magnetometer in the shipboard environment is about 2×10^{-9} Am². For a split core, the large volume of core material within the sensing region of the magnetometer (~100 cm³) permits accurate measurements of remanent intensities greater than about 2×10^{-5} A/m. For discrete samples, which typically have volumes of 6–10 cm³, the magnetometer can accurately measure samples with intensities greater than about 4×10^{-4} A/m. The magnetometer is scheduled for tuning following Leg 186, so this noise level may be reduced for future legs.

The natural remanent magnetization (NRM) before and after AF demagnetization was routinely measured for all archive-half sections at 2- or 5-cm intervals. In interpreting the data, we avoided using the measurements within 5 cm from the ends of each section, although we saved these values for future studies that might wish to deconvolve the

remanence signal. Alternating-field demagnetizations were applied at 10, 20, and 30 mT on all sections. For a few sections from each site, we did detailed demagnetization in 5-mT steps from 0 to 60 or 70 mT.

Most of the discrete samples were also measured with the cryogenic magnetometer. Typically samples were demagnetized in 10-mT steps from 0 to 60 mT, though more detailed demagnetization was conducted on a few of the samples. A few samples were stepwise thermally demagnetized, typically at 30°C steps, using a thermal demagnetizer (Schonsted Instrument Co., Model TSD-1), and then measured with the cryogenic magnetometer.

An automatic portable spinner magnetometer (Niitsuma and Koyama, 1994) was used to measure remanence magnetization of some of the discrete samples collected during Leg 186. The noise level of this magnetometer is roughly equivalent to that of the cryogenic magnetometer for the 7-cm³ discrete samples, when 10 repeat measurements are averaged. This magnetometer is equipped with an AF demagnetizer, an anhysteretic remanent magnetizer, and magnetic susceptibility anisotropy meter. Detailed stepwise AF demagnetizations were performed using this automatic magnetometer to compare with the long-core data. About one sample per section in the APC and one sample per core in the XCB and RCB intervals were measured with this portable unit.

To investigate rock magnetic characteristics of some of the discrete samples, ARM and IRM experiments were conducted and then the samples were measured using the cryogenic magnetometer. The DTECH AF demagnetizer (Model D2000) was used to impart ARMs to discrete samples, using a 100-mT peak AF and a 0.05-mT direct current field. We then progressively demagnetized the samples at 10-mT increments from 0 to 60 mT using the cryogenic magnetometer. IRMs were imparted to the discrete samples using the Analytical Services Company Impulse Magnetizer (Model IM-10) with a DC field of 1000 mT. The samples were then stepwise AF demagnetized at 10-mT increments from 0 to 60 mT using the cryogenic magnetometer. In addition, we conducted IRM acquisition experiments and thermal demagnetization of IRMs on a few samples.

Low-field magnetic susceptibility was measured for all whole-core sections as part of the MST analysis (see **“Physical Properties,”** p. 18). The MST susceptibility meter (a Bartington Model MS-2 with an MS2C sensor; inner coil diameter = 88 mm; operating frequency = 0.565 kHz) has a nominal resolution of 2×10^{-6} SI (Blum, 1997). Susceptibility was determined at 2-cm intervals using a 1-s integration time and a 4-s period. The “units” option was set on SI units and the values were stored in the Janus database in raw meter units. For conversion to true SI volume susceptibilities, these should be multiplied by 10^{-5} , and then should be multiplied by a correction factor to take into account the volume of material that passed through the susceptibility coils. Except for measurements near the ends of each section, this factor for a standard ODP core is about 0.7 (Blum, 1997). No correction was applied for any figures illustrating magnetic susceptibilities in this volume. Hence, the units are given as raw meter values. Magnetic susceptibility of discrete samples obtained from the working half was measured using a Bartington MS2 susceptibility meter with a dual frequency MS1B Sensor. Magnetic susceptibility was used as a first-order measure of the amount of ferrimagnetic material and as a correlation tool.

Core Orientation

The standard ODP paleomagnetic coordinate system was used. In this system, +x is vertical upward from the split-core surface of archive halves, +y is left along the split-core surface when looking upcore, and +z is downcore (Fig. F7).

Most of the few APC cores collected during Leg 186 were azimuthally oriented using the Tensor tool. The Tensor tool consists of a three-component fluxgate magnetometer and a three-component accelerometer rigidly attached to the core barrel. The information from both sets of sensors allows the azimuth and dip of the hole to be measured as well as the azimuth of the double-line orientation mark on the core liner. Orientation is not usually attempted for the top two or three cores (~20–30 mbsf) until the bottom hole assembly is sufficiently stabilized in the sediment. The output from the Tensor tool, which contains a variety of angles including the inclination angle of the hole and the magnetic toolface (MTF) angle, is archived in the Janus database. The inclination angle of the hole is a measure of deviation of the hole from vertical and the MTF angle gives the angle between the magnetic north and the double-line orientation mark on the core liner. The core liner is always cut such that the double lines are at the bottom of the working half.

Using the ODP coordinate system for the archive and working halves or for samples taken from them, the measured remanent declination can then be corrected to magnetic north by adding the MTF angle and can be further corrected to true north by adding the deviation of magnetic north from true north, the latter of which can be estimated from the International Geomagnetic Reference Field (IGRF) coefficients. The equation is

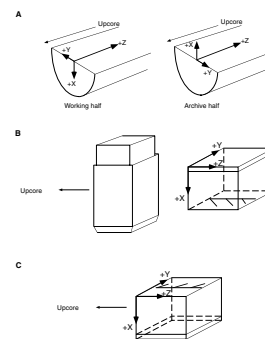
$$D_T = D_O + A_{MTF} + M_{IGRF}, \quad (1)$$

where D_T is the Tensor tool corrected or true declination, D_O is the observed declination output from the cryogenic magnetometer, A_{MTF} is the MTF angle, and M_{IGRF} is the deviation of magnetic north from true north. At Sites 1150 and 1151, we used -7.7° for the M_{IGRF} correction. Specific details concerning orientation of APC cores from these sites are discussed in the site chapters.

Sampling Methods and Orientations for Discrete Samples

Oriented discrete samples were taken from the working half of each section (typically one per section for shipboard analyses) using a cube with flattened corners (the Japanese paleomagnetism cube) and a stainless-steel extruder or using a 2 cm × 2 cm × 2 cm plastic cube (the French cube) and an aluminum extruder. The volume of both cubes is ~7 cm³. In lithified intervals, we used the rock saw to cut the sample, which was then placed in the Japanese cube such that the orientation of the sample in the plastic cube was the same as would have been attained with the extruder. Nine samples from APC cores were collected by pressing the Japanese cube directly into the sediment. The two sampling methods yield a 180° difference in the orientations of both the +x and +y axes (Fig. F7); therefore, we have carefully marked the labels on

F7. Coordinate systems for samples, p. 43.



those eight sample cubes with a red dot. In all cases, the arrow on the cubes points upcore.

About 10% of the discrete samples were placed in the Japanese cubes and were measured with the spinner magnetometer. These data are not available in the Janus database but are provided in tables within the site chapters. The remaining samples, including all of those in the French cubes, were measured in the cryogenic magnetometer using a tray with seven sample holders. The first sample holder is 20 cm from the top of the tray, and the others are spaced every 20 cm down the tray. To properly orient the French cube in the standard ODP magnetic coordinate system would require that the lid of the cube be placed down in the sample holders. Owing to the tight fit, which can damage the sample holders, we instead placed the bottom of the cube in the sample holder. Thus, the declination is rotated 180° from its proper position. In all plots, we have made this correction, but the raw data in the Janus database are uncorrected. We provide a table of the corrected values in the site chapters.

Magnetostratigraphy

We encountered several types of secondary magnetization acquired during coring, which sometimes hampered magnetostratigraphic interpretation. The most common was a steep downward-pointing overprint attributed to the drill string. For the Leg 186 cores, we also observed a slight bias for 0° declinations, which has been observed on many previous cruises and has been interpreted as a radially-inward overprint. Other overprints related to reduction diagenesis or tectonic deformation were observed. Details of these and other magnetic complexities are presented in the site chapters.

Where AF demagnetization successfully isolated the characteristic component of remanence, paleomagnetic inclinations were used to define polarity zones. The declination provided additional constraints for those few APC cores oriented with the Tensor tool. Ages for reversals (Fig. F6) are from the revised Cenozoic time scale of Cande and Kent (1995), as presented in Berggren et al. (1995).

GEOCHEMISTRY

The shipboard geochemistry program for Leg 186 included (1) real-time monitoring of volatile hydrocarbons for safety and pollution prevention as required by ODP regulations; (2) measurement of inorganic carbon and carbonate content of sediments; (3) elemental analyses of total nitrogen, hydrogen, sulfur, and carbon; and (4) measurement in interstitial waters of salinity, alkalinity, pH, and concentration of major dissolved ionic species (i.e., chloride, sulfate, ammonium, sodium, potassium, magnesium, calcium, lithium, and strontium). All methods and instruments used during Leg 186 are described in detail by Emeis and Kvenvolden (1986), Kvenvolden and McDonald (1986), and in the "Explanatory Notes" chapter of the Leg 156 *Initial Reports* volume (Shipboard Scientific Party, 1995).

Volatile Hydrocarbons

The main focus of shipboard organic geochemical analyses is to monitor abundances of the light hydrocarbons methane (C₁), ethane

(C₂), ethylene (C₂₌), propane (C₃), and propylene (C₃₌) to assess possible hazardous hydrocarbon accumulations at depth. These accumulations can potentially pollute the environment and/or put the ship in risk. The assessment of potential hydrocarbon accumulations is based on the C₁/C₂ and C₁/C₃ values. As a general rule, values less than 200 for C₁/C₂ and 2000 for C₁/C₃ justify caution. These values, however, are also related to depth and temperature (Stein et al., 1995; JOIDES Journal, 1992) and should be used only as a guideline. Any decision regarding stopping the drilling operation should be determined based on those ratios, in conjunction with deviations from usual trends of these values with depth, coupled with significantly higher abundances of heavier hydrocarbons.

During Leg 186, concentrations of light hydrocarbon gases were monitored for each core following the standard headspace sampling method described by Kvenvolden and McDonald (1986). Briefly, immediately after the core was retrieved and cut into 150-cm sections, a No. 6 cork borer was used to obtain a sediment sample from the top of one of the sections. This ~5-cm³ sediment sample was placed in a 21.5-cm³ glass serum vial and sealed with a septum and metal crimp cap. When consolidated or lithified samples were encountered, chips of material were placed in the vial and sealed. Before gas analysis, sediment samples were heated in an oven at 60°C for 20 min. A gas-tight syringe and needle was then used to extract approximately 5.0 mL of headspace gas. When gas pockets were encountered, free-gas samples were collected by penetrating the liner with a syringe connected to a penetration tool.

Constituents of the headspace and free-gas samples were routinely analyzed using a Hewlett-Packard (HP) 6890 gas chromatograph (GC) equipped with a 0.25-cm³ sample loop, an 8 × 1/8-inch stainless steel column packed with HaySep R (80/100 mesh), and a flame ionization detector (FID). The carrier gas was helium with a flow of 30 mL/min. The initial temperature of the GC oven was held at 120°C. Data acquisition and processing were performed by HP Chemstation version 5.04. Free-gas samples were also analyzed with a natural gas analyzer (NGA) to quantify light hydrocarbons (methane to hexane) and nonhydrocarbon gases including nitrogen, oxygen, and carbon dioxide. The NGA system consists of a Hewlett-Packard 6890 GC equipped with two different columns and detectors. Hydrocarbons were analyzed with a 60 m × 0.32 mm SGE 50QC3 BP-1 capillary column and an FID. The initial temperature of the GC oven was held constant at 40°C for 10 min and then increased to 100°C at 10°C/min. Helium was used as the carrier gas at a flow of 1.5 mL/min. Nonhydrocarbon gases were analyzed isothermally (150°C) using a sequence of packed columns: a 6-in stainless steel HaySep R (80/100 mesh) column connected to a 3-ft molecular sieve 13 × (60/80 mesh) column, and a 6-in stainless steel Poropak T (50/80 mesh) column. A thermal conductivity detector (TCD) was used for detection. Helium was the carrier gas. Data acquisition and processing were performed by HP Chemstation software. Chromatographic response was calibrated against authentic standards and the results reported as parts per million (ppm).

Inorganic Carbon

Inorganic carbon was determined at a frequency of three samples per core using a Coulometrics 5011 carbon dioxide coulometer equipped with a System 140 carbonate carbon analyzer. Aliquots of about 10 mg

of freeze-dried, ground sediment were weighed and reacted with 2N HCl to liberate CO₂. The evolved CO₂ was coulometrically titrated using monoethanolamine. Pure calcite standards were used for quantification. Carbonate content (in weight percent, wt%) was calculated from the inorganic carbon (IC) content assuming that all the carbonate was present as calcite using the following equation:

$$\text{CaCO}_3 \text{ (wt\%)} = \text{IC (wt\%)} \times 8.332. \quad (2)$$

Elemental Analysis

Total carbon (TC), hydrogen, nitrogen, and sulfur were analyzed using a Carlo Erba 1500 CNS Analyzer at a frequency of one sample per core. About 10 mg of freeze-dried, ground sediment was weighed and combusted with a V₂O₅ catalyst at 1000°C in a stream of oxygen. Nitrogen oxides were reduced to N₂ and the mixture of evolved gases was separated by gas chromatography. Detection of separated gases was performed by TCD, using sulfanilamide as a calibration standard. The amount of total organic carbon (TOC) was calculated as the difference between TC and IC as follows:

$$\text{TOC (wt\%)} = \text{TC} - \text{IC}. \quad (3)$$

Atomic C/N values were calculated from TOC and total nitrogen concentrations.

Interstitial Water Samples

Interstitial water samples were extracted from 5- to 10-cm-long whole-round sections cut immediately after core retrieval on deck. During Leg 186, samples were gathered at a frequency of one per core for the first 30 m, and one every three cores until IW could no longer be extracted. After extruding the sediment from the core liner, the surface of each whole-round section was carefully scraped with a spatula to remove potential contamination. IW samples were extracted by placing the sediment in a titanium squeezer and applying pressures as high as 40,000 lb (~4150 psi) using a Carver hydraulic press. Water samples were collected into acid-cleaned plastic syringes and filtered through sterile 0.45-µm Gelman polysulfone disposable filters. Samples for shipboard analyses were stored in plastic vials and those for shore-based analyses were stored in heat-sealed acid-washed plastic tubes and/or glass vials.

Analyses of IW followed the procedures outlined by Gieskes et al. (1991). Salinity was measured with a Goldberg optical handheld refractometer. The pH and alkalinity were measured by Gran titration with a Brinkmann pH electrode and a Metrohm autotitrator. The Cl⁻ concentration was measured by titration. Concentrations of NH₄⁺ were measured by spectrophotometric methods with a Milton Roy Spectronic 301 spectrophotometer. Concentrations of K⁺, Mg²⁺, Na⁺, Ca²⁺, and SO₄²⁻ were measured by ion chromatography using a Dionex DX-120 instrument. Concentrations of Li⁺ and Sr²⁺ were measured by flame atomic absorption spectrophotometry using a Varian SpectrAA-20.

Analytical precision was determined by replicate analyses of natural samples and by reanalyzing standards as unknowns. Values of precision, expressed as percent of the measured value, are as follows for the

respective constituents: alkalinity, <1.5%; Cl⁻, 0.4%; Ca²⁺, <1%; Mg²⁺, 0.5%; NH₄⁺, ~5%; K⁺, <3%; SO₄²⁻, <4%; and Na⁺, <5%.

PHYSICAL PROPERTIES

Objectives

The standard procedures for shipboard measurements of physical properties provide insights to variations in the core material characteristics. The general objectives for the physical properties group were to

1. Collect comprehensive physical properties data sets for constructing a complete stratigraphic section and determining lithologic units;
2. Determine physical and deformational properties of lithologic units for defining erosional unconformities, delineating the consolidation degree of cored sections, and estimating mass accumulation rates;
3. Cross-correlate and calibrate shipboard analyses of physical properties with other shipboard analyses. Physical properties samples were commonly taken next to shipboard carbonate and XRD samples;
4. Integrate core, downhole logging, and seismic reflection data. Bulk density, porosity, compressional velocity and natural gamma radiation (NGR) data from core sampling are all valuable for core-log integration; and
5. Cross-correlate results from Sites 1150 and 1151 with the DSDP Sites 438, 439, and 584 that also are located on the continental slope of the Japan Trench.

In addition, physical properties serve to address basic questions related to the underlying themes of this cruise. For example, how do physical properties of sediment and sedimentary rock differ for seismic and aseismic segments of the continental slope?

Except for data from Holes 1151C and 1151D, physical properties data were acquired after the cores had equilibrated to ambient laboratory room temperature (18°–25°C, measured in the top of the section). Nondestructive measurements were made on whole-round core sections with the MST, which acquires magnetic susceptibility, bulk density, compressional *P*-wave velocity, and NGR data, and with a needle probe that measures thermal conductivity. Destructive measurements were conducted on split-core sections with relatively unlithified sediments (compressional *P*-wave velocity and shear strength) and on discrete samples (index properties and compressional *P*-wave velocities). A detailed description of the principles for these techniques is given in the ODP physical properties handbook (Blum, 1997).

Nondestructive Measurements

Multisensor Track

The MST incorporates the magnetic susceptibility, gamma-ray attenuation (GRA), *P*-wave logger (PWL), and NGR devices. Individual whole-round core sections are scanned by the four sensors and sampled at constant intervals and periods, from the top to bottom depth of the

section. Each section was oriented so that the working half was facing up. This provided internal consistency for individual cores, but not between different cores because their orientation to north was not known. Raw data from MST measurements are stored in the Janus database, whereas the additional corrections of the data (see below) are not.

Magnetic susceptibility was measured with a 2-cm sampling interval on all cores recovered in Site 1150 and Hole 1151A, and with a 5-cm sampling interval on cores from Holes 1151C and 1151D. The 1.0 (1-s integration time) range on the Bartington meter (Model MS2C), which has an 8.8-cm diameter loop, was used and the sampling period was 4 s. Magnetic susceptibility aids in the detection of variations in the concentrations of magnetic minerals associated with lithologic changes. The quality of the data is degraded in RCB sections if the core liner is not completely filled and/or the core is disturbed. However, general downhole trends may still be used for core-log correlation. The precision and accuracy of magnetic susceptibility measurements are 2×10^{-6} (SI) and 5%, respectively (Blum, 1997). The results of magnetic susceptibility measurements are included in the site chapters.

The GRA measured bulk density at 2-cm intervals (in Site 1150 and Hole 1151A) and at 5-cm intervals (in Holes 1151C and 1151D) during 4-s-long sampling periods. The attenuation of gamma rays through the cores are compared with attenuation through aluminum and water standards, and the GRA bulk density is calculated assuming a constant core diameter (Boyce, 1976). Gamma-ray attenuation data are most reliable in undisturbed cores, whereas bulk density tends to be underestimated in sections with incompletely filled core liner. In RCB cores, GRA bulk density measurements were corrected to account for their smaller core diameters (Blum, 1997):

$$r_c = r \cdot d_c / d, \quad (4)$$

where r_c is corrected bulk density, r is measured GRA bulk density, d_c is the corrected core diameter, and d is the assumed core diameter (66 mm). All density data were edited by removing values less than 1.0 g/cm³ (i.e., density of pure water). The precision of GRA measurements depends on the count rate, sampling period, and number of standard deviations for the normal distribution. Counting rates of 20,000 counts per second (cps) and sampling periods of 4 s correspond to a statistical error of less than 0.4% for a 68% confidence interval (Blum, 1997). The GRA sensor was generally calibrated every 2 or 3 days with a distilled-water standard.

The PWL transmits a 500-kHz compressional wave (*P*-wave) pulse through the core at a repetition rate of 1 kHz. The transmitting and receiving transducers are aligned normal to the core axis (horizontal direction). A pair of displacement transducers monitors the separation between the *P*-wave transducers. Measurements were taken at 2-cm intervals (in Site 1150) and at 5-cm intervals (in Site 1151) during a sampling period of 4 s. Only continuous cores that filled their core liners were measured (i.e., only APC cores). Corrections were made for the *P*-wave traveltime through the liner ($2 \cdot d_{\text{liner}} = 5.08$ mm and $v_{\text{liner}} = 1990$ m/s). The velocity data were edited in two steps. First, data with a signal quality less than 40 were removed. The signal quality is a measure of how well the acoustic signal traveled through the core, and it can vary from 0 to 255. Second, velocity values less than 1450 m/s (i.e., the velocity of seawater at 0°C) were deleted. Velocities from sediment cores

from below a few hundred meters are typically compatible with downhole log measurements within less than 3%, whereas shallower core measurements tend to be as much as 5% lower than the corresponding logs (Blum, 1997). The PWL sensor was calibrated approximately once per week.

Natural gamma radiation activity was measured at 20-cm intervals in each section, with a sampling period of 20 s. Data from 2048 energy channels were collected and archived, and counts were summed over the range from 200 to 3000 keV. This integration range allows for comparison of the trends of NGR data with those of downhole logging data, although the two methods use different units (cps and gAPI [gamma-ray American Petroleum Institute], respectively). Before starting measurements, the four sensor gains were calibrated so that the combined thorium peak was as sharp as the individual peaks when the other three were disabled. The multichannel analyzer was calibrated by assigning certain channels to the characteristic energies of ^{40}K and the main peak of ^{232}Th (Ocean Drilling Program, 1996). Furthermore, a background radiation of 12.27 cps was measured using a core liner filled with distilled water and a 30-s sampling period. The axial resolution is about 12 cm due to the geometry of the device, and the error of the system (estimated from reference values) varies from 3% to 7% (Blum, 1997). Corrections for sampling volume as proposed by Hoppie et al. (1994) were not made; thus, the data are reported in counts per second.

Thermal Conductivity

Thermal conductivity (k) is the rate at which heat is transmitted by molecular conduction. Thermal conductivity and temperature measurements of sediments and rock sections are used to determine heat flow. Heat flow is not only characteristic of the material, but also an indicator of type and age of ocean crust, and fluid circulation processes at shallow and great depth (Blum, 1997).

Thermal conductivity was only measured in soft sediments using the needle-probe method in full-space configuration (von Herzen and Maxwell, 1959). Data were typically acquired once in every core. The mean error associated with these determinations is estimated to ± 0.2 W/(m·K), or less than 15% (Blum, 1997).

A needle probe containing a heater wire and a calibrated thermistor was inserted into the sediment through a small hole drilled in the core liner before the sections were split. At the beginning of each test, temperatures in the samples were monitored without applying current to the heating element to verify that temperature drift was < 0.04 K/min. The heater was then turned on and the temperature rise in the probes recorded. After heating for about 60 s, the needle probe behaves nearly as a line source with constant heat generation per unit length. Temperatures recorded between 60 and 240 s were fit to the following equation using the least-squares method (von Herzen and Maxwell, 1959):

$$T(t) = [q / (4 \cdot p \cdot k)] \cdot \ln(t) + L(t), \quad (5)$$

where k is apparent thermal conductivity (W/[m·K]), T is temperature (K), t is time (s), and q is heat input per unit length of wire (W/m). The term $L(t)$ corrects for temperature drift and is described by

$$L(t) = A \cdot t + T_e, \quad (6)$$

where A is rate of temperature change and T_e is equilibrium temperature. Thus, $L(t)$ corrects for the background temperature drift, systematic instrumental errors, probe response, and sample geometry. The best fit to the data determines the unknown terms k and A .

Destructive Measurements

All measurements were made close to each other. Samples were taken from approximately the same depth interval of each section to provide a uniform sampling frequency. Disturbed core sections (i.e., sections with drilling biscuits and other drilling disturbances) were avoided.

Compressional (*P*-Wave) Velocity

P-wave velocity was measured using the PWS1, PWS2 and PWS3 systems. The choice of method and sampling frequency of discrete *P*-wave velocity measurements depends on the degree of induration of the sediment and the recovery. In soft sediments, *P*-wave velocity is measured by PWS1 and PWS2 systems, whereas only PWS3 is used in lithified sediments. Generally, *P*-wave velocity was measured once per section.

PWS1 and PWS2 consists of two pairs of digital sound velocimeters. The pairs are aligned parallel (PWS1; vertical) and normal (PWS2; horizontal) to the core axis. The transducer pairs of PWS1 has a fixed spacing of 7 cm, whereas PWS2 has a fixed spacing of 3.5 cm. An acoustic signal of 500 kHz is emitted and received by the transducers. The signal is digitized in an oscilloscope, from which the first arrival waveform can be picked and the *P*-wave velocity is obtained by dividing the spacing of the transducers with the first arrival time. The temperature of the sediment was measured adjacent to the PWS1 measurement in soft lithologies.

An improved Hamilton Frame system (PWS3) is used to measure *P*-wave velocity through the split core (horizontal direction), on indurated core pieces (horizontal direction) and cylindrical minicores (vertical and two orthogonal horizontal directions). Only coherent pieces that could be cut into minicores were selected for measurements. Hence, sampling tended to favor indurated and nonfractured sections. The PWS3 emits a 500 kHz *P*-wave pulse through the sediment. The sample thickness (and transducer separation) is measured with a digital caliper that is mounted on the transducers. The distance between the two transducers is decreased until a measurable waveform appears on the oscilloscope. To improve the coupling between transducer and sample, distilled water was applied between the sample and the transducer heads. Zero traveltimes were measured with a series of polycarbonate standards of known length. All measurements on split cores were corrected for the additional traveltime passing through the core-liner ($d_{\text{liner}} = 2.54$ mm and $v_{\text{liner}} = 1990$ m/s).

The approach to measure *P*-wave velocity in two or three directions on minicores provides a measure of the acoustic anisotropy (A_{12}) of the sediments (Carlson and Christensen, 1977):

$$A_{12} = 2 \cdot (V_1 - V_2) / (V_1 + V_2), \quad (7)$$

where, V_1 is V_x or V_y , and V_2 is V_x , V_y , or V_z . Horizontal velocity is measured in two orthogonal directions (V_x and V_y) perpendicular to the core axis, and vertical velocity (V_z) is measured parallel to the core axis. The

spatial relationships between the x, y, and z axes are illustrated in figure 1-1 of Blum (1997).

An estimate of the azimuthal influence on the magnitude of horizontal anisotropy (A_{xy}) was obtained from paleomagnetic declination data (see "**Paleomagnetism**," p. 12). Directional paleomagnetic data were acquired from all archive half cores with a sampling frequency of 2- to 5-cm after AF demagnetization of 30 mT. The mean declination and 95% confidence limit (α_{95}) of the core section from which the minicore was taken were calculated with the program Direction (a stereographic calculation and plot program). The 95% confidence limit (α_{95}) of Fisher statistics is a measure of the precision with which the true mean direction has been estimated and analogous to a 95% probability level of the estimated standard error of the mean of Gaussian statistics. The orientations of horizontal velocities were placed into geographical coordinates by a rotation equivalent to the observed declination (e.g., $V_x^{\text{azimuth}} = 50^\circ\text{N}$ and $V_y^{\text{azimuth}} = 140^\circ\text{N}$ for a declination of 50°N , and $V_x^{\text{azimuth}} = 100^\circ\text{N}$ and $V_y^{\text{azimuth}} = 10^\circ\text{N}$ for a declination of 280°N).

Undrained Shear Strength

The peak undrained shear strength (S_u) generally was measured once per split core section, using a Wykeham-Farrance motorized vane shear apparatus following the procedures of Boyce (1977). The vane rotation rate was set to $90^\circ/\text{min}$, and the vane used for all measurements had a 1:1 blade ratio with a dimension of 1.28 cm. This instrument measures the torque and strain at the vane shaft using a torque transducer and potentiometer, respectively. Output for torque and strain are recorded on a Hewlett-Packard X-Y recorder. The undrained shear strength (i.e., the peak strength) is determined from the torque vs. strain plot and reported in kilopascals (kPa).

In the interpretation of shear vane measurements, it is assumed that a cylinder of sediment is uniformly sheared around the axis of the vane in an undrained condition, with cohesion as the principal contributor to shear strength. Departures from this assumption include progressive cracking within and outside of the failing specimen, uplift of the failing core cylinder, drainage of local pore pressures, and stick-slip behavior. Consequently, shear vane measurements are only conducted in soft and clay-rich sediments.

A pocket penetrometer is used for measurements in stiffer sediments. The pocket penetrometer is a small, flat-footed cylindrical probe that is pushed into the split core to a depth of 6.4 mm. The resulting resistance is the unconfined compressive strength, or $2 \times S_u$. A scale directly reads out in units of kilograms per cubic centimeter. The value of unconfined compression were converted to values of S_u and reported in units of kilopascals.

Index Properties

Samples of approximately 10 cm^3 were taken from the fresh split core for determination of index properties. For Leg 186, measurements of the wet and dry mass and the dry volume of a sample were used to determine the index properties (i.e., Method C; Blum, 1997). Sample mass was determined with an error within 0.1% using two Scitech electronic balances. The balance is equipped with a computer averaging system that corrected for ship accelerations. The sample mass was counterbal-

anced by a known mass such that the mass differentials were less than about 10 g. Dry weight and volume measurements were performed after the samples were oven dried at $105^\circ \pm 5^\circ\text{C}$ for 24 hr and allowed to cool in a desiccator. The main problem with this drying temperature is that chemically bound water in clay minerals is largely lost in addition to interstitial water. Dry volume of samples were determined using a Quantachrome Penta-Pycnometer, which is a helium-displacement pycnometer. Sample volumes were determined at least five times, until readings were consistent (i.e., standard deviation = $< 0.01\%$). A standard reference volume was run with each group of samples during the measurements and rotated among the cells to check for instrument drift and systematic error. This exercise demonstrated that the measured volumes had a precision of about 0.02 cm^3 . The sample beakers used for discrete determinations of index properties were calibrated before the cruise.

The following index properties were calculated: water content (based on total wet mass and mass of solids), bulk density, dry density, grain density, porosity, and void ratio. Table T5 lists the measured parameters, assumptions, and relationships of index properties calculations, which were corrected for salinity and density of the pore water following Boyce (1976). The determination of water content followed the methods of the American Society for Testing and Materials (ASTM) designation (D) 2216 (ASTM, 1989). In situ measurements of the salinity of pore water (see “Geochemistry,” p. 37, in the “Site 1150” chapter and “Geochemistry,” p. 25, in the “Site 1151” chapter) showed that the salinity was significantly lower than standard salinity used for automatic calculations ($S = 0.035$). Therefore, index properties were recalculated using in situ values of salinity and density of the pore water. The pore water density is a function of temperature, salinity, and pressure (Blum, 1997). At laboratory conditions (20°C , 1 bar), we derived the following relationship between pore-water density (ρ_{pw}) and pore-water salinity (S) by fitting the data to a line (see fig. 2-1 of Blum, 1997):

$$\rho_{pw} = 0.998 + 7.7143 \cdot S. \quad (8)$$

To allow cross-examination of the data for internal consistency, values of porosity, dry density, and void ratio were calculated indirectly from the other index properties (see Table T5 for definition of terms):

$$\eta = 100 \cdot [(\rho_g/\rho_{pw} - \rho_b) / (\rho_g/\rho_{pw} - \rho_{pw})], \quad (9)$$

$$\eta = W_s \cdot \rho_b / [(1 + W_s/100) \cdot \rho_{pw}], \quad (10)$$

$$\rho_d = \rho_{pw} + \eta/W_s, \text{ and} \quad (11)$$

$$e = \rho_g \cdot W_s / (\rho_{pw} \cdot 100). \quad (12)$$

The magnitude of total vertical stress (σ_v) and effective vertical stress (σ'_v) from the sediment section was calculated by integrating bulk density (ρ_b), water density (ρ_{pw}), and porosity (η) data with depth from core and log measurements:

$$\sigma_v = g \cdot \int (\rho_b \cdot z) dz, \text{ and} \quad (13)$$

$$\sigma'_v = g \cdot \int [(\rho_b - \rho_{pw} \cdot \eta/100) \cdot z] dz, \quad (14)$$

T5. Measured and calculated parameters, assumptions, and relationships for index properties calculations, p. 49.

where g = the acceleration of gravity at the Earth's surface (9.802 m/s^2) and z = depth.

DOWNHOLE MEASUREMENTS

Introduction

Downhole logs are continuous records of physical, chemical, and structural properties of the formation penetrated by a borehole. The logs are made using a variety of probes combined into several tool strings. These strings are lowered down the hole on a heave-compensated electrical wireline and then pulled up at a constant speed to provide continuous measurements as a function of depth. Logs can be used to interpret the stratigraphy, lithology, mineralogy, and structure of the penetrated formations. Where core recovery is incomplete or disturbed, log data may provide the only way to characterize the borehole section. Where core recovery is good, log and core data complement one another and may be interpreted jointly. Finally, downhole logs are sensitive to formation properties on a scale that is intermediate between those obtained from laboratory measurements on core samples and geophysical surveys.

Three logging tool strings were used during Leg 186: the triple combination logging tool (triple combo)/temperature, the Formation MicroScanner (FMS)/sonic, and the borehole televiewer (BHTV). In addition to wireline logs, in situ temperature measurements were made with the APC temperature tool and Davis-Villinger temperature probe (DVTP).

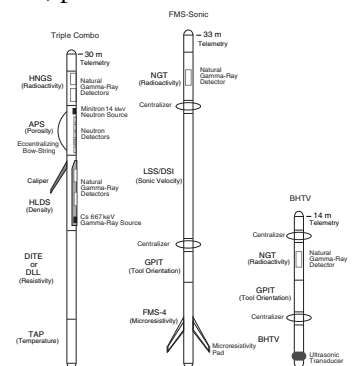
Logging Tools

The tool strings used on Leg 186 were

1. The triple combo tool string (resistivity, density, and porosity; see Fig. F8) consists of the accelerator porosity sonde (APS), the hostile environment lithodensity sonde (HLDS), and the phasor dual induction-spherically focused resistivity tool (DITE-SFL), depending on formation resistivity. The hostile environment spectral natural gamma-ray sonde (HNGS) was included at the top of the string, and the Lamont-Doherty Earth Observatory temperature/acceleration/pressure tool (LDEO-TAP) at the bottom.
2. The FMS/sonic tool string (Fig. F8) consists of the FMS, the general purpose inclinometer tool (GPIT), and a sonic sonde. The dipole shear sonic imager (DSI) and the long-spaced sonic imager (LSS) were used during Leg 186. The natural gamma-ray tool (NGT) was included at the top of this tool string.
3. The BHTV tool string (Fig. F8) consists of the BHTV and the GPIT. The NGT was included at the top of this tool string. This string was used to address the specific objectives of Leg 186: to constrain the borehole condition such as hole geometries, stress, and stabilities in the lower part of the borehole, where we expected to install downhole instruments.

Each tool string includes a telemetry cartridge for communicating through the wireline with the logging laboratory on the drillship and a

F8. Leg 186 tool string configurations, p. 44.



natural gamma-ray sonde that is used to identify lithologic markers, providing a common reference for correlation and depth shifting between multiple logging runs. Logging runs are typically conducted at 250–275 m/hr.

The logging tools are briefly described below, and their operating principles, applications, and approximate vertical resolution are summarized in Table T6. More detailed information on individual tools and their geological applications may be found in Ellis (1987), Goldberg (1997), Lovell et al. (1998), Rider (1996), Schlumberger (1989, 1994), Serra (1984, 1986, 1989), and the LDEO-Borehole Research Group Wireline Logging Services Guide (1994).

T6. Leg 186 logging tools and their applications, p. 50.

Natural Radioactivity

Two spectral gamma-ray tools were used to measure and classify natural radioactivity in the formation: the HNGS and the NGT. The NGT uses a sodium iodide scintillation detector and five-window spectroscopy to determine concentrations of K (in weight percent), Th (in parts per million), and U (in parts per million), the three elements whose isotopes dominate the natural radiation spectrum. The HNGS is similar to the NGT, but it uses two bismuth germanate scintillation detectors for a significantly improved tool precision. Spectral analysis in the HNGS filters out gamma-ray energies below 500 keV, eliminating sensitivity to bentonite or KCl in the drilling mud and improving measurement accuracy.

The NGT response is sensitive to the borehole diameter and the weight of the drilling mud, which is controlled by the concentration of bentonite or KCl. These effects are routinely corrected for during post-cruise processing at LDEO.

Density

Formation density was determined from the density of electrons in the formation, which was measured with the HLDS. The sonde contains a radioactive cesium (^{137}Cs) gamma-ray source (622 keV) and far and near gamma-ray detectors mounted on a shielded skid that is pressed against the borehole wall by a hydraulically activated eccentralizing arm. Gamma rays emitted by the source experience Compton scattering, which involves the transfer of energy from gamma rays to the electrons in the formation via elastic collision. The number of scattered gamma rays that reach the detectors is directly related to the number of electrons in the formation, which is in turn related to bulk density. Porosity may also be derived from this bulk density if the grain density is known.

The HLDS also measures the photoelectric effect factor (PEF) caused by absorption of low-energy gamma rays. Photoelectric absorption occurs when gamma rays reach less than 150 keV after being repeatedly scattered by electrons in the formation. Because PEF depends on the atomic number of the elements in the formation, it varies according to the chemical composition and is essentially independent of porosity. For example, the PEF of pure calcite = 5.08 barn/e⁻; illite = 3.03 barn/e⁻; quartz = 1.81 barn/e⁻; and kaolinite = 1.49 barn/e⁻. Photoelectric effect factor values can be used in combination with NGT curves to identify different types of clay minerals. Coupling between the tool and borehole wall is essential for good HLDS logs. Poor contact results in underestimation of density values. Poor contact may occur when the

borehole diameter is greater than the length of the eccentricizing arm (e.g., for borehole diameters >48 cm).

The depth of investigation of the lithodensity tool is of the order of tens of centimeters, depending on the density of the rock.

Porosity

Formation porosity was measured with the APS. The sonde incorporates a minitron neutron generator which produces fast (14.4 MeV) neutrons, and five neutron detectors (four epithermal and one thermal) positioned at different spacings. The tool is pressed against the borehole wall by an eccentricizing bow-spring. Emitted neutrons are slowed down by collisions. The amount of energy lost per collision depends on the relative mass of the nucleus with which the neutron collides. The greater energy loss occurs when the neutron strikes a nucleus nearly equal to its own mass, such as hydrogen, which mainly is present in the pore water. The neutron detectors record both the numbers of neutrons arriving at various distances from the source and neutron arrival times which act as a measure of formation porosity. However, because hydrogen bound in minerals such as clays or in hydrocarbons also contributes to the measurement, the raw porosity is often overestimated.

Electrical Resistivity

The DITE was used to measure the formation electrical resistivity. The DITE provides three measures of electrical resistivity, each with a different depth of investigation into the formation. Deep and medium penetration measurements are made inductively using transmitter coils that are energized with high-frequency alternating currents, creating time-varying magnetic fields that induce secondary Foucault currents in the formation. The strength of these induced ground currents is inversely proportional to the resistivity of the formation through which they circulate, as are the secondary inductive fields that they create. The amplitude and phase of the secondary magnetic fields, measured with receiving coils, are used as a proxy for the formation resistivity. Shallow penetration measurements with a high vertical resolution are made with a spherically focused laterolog. This measures the current necessary to maintain a constant voltage drop across a small fixed interval. Because of the inductive nature of the deep and medium penetration measurements, DITE logs are accurate only for formations with resistivities less than about 100 Ωm , such as sediments. In more resistive formations, measurement error becomes significant (>20%), and it is more suitable to use the dual laterolog (Schlumberger, 1989).

For the deep measurement, both focusing and measurement currents return to a remote electrode on the surface; thus, the depth of investigation is considerable, and the effect of borehole conductivity and of adjacent formations is reduced. In the shallow laterolog, the return electrodes that measure the bucking currents are located on the sonde; therefore, the current sheet retains focus over a shorter distance than the deep laterolog. Fracture porosity can be estimated from the separation between the deep and shallow measurements based on the observation that the former is sensitive to the presence of horizontal conductive fractures only, whereas the latter responds to both horizontal and vertical conductive structures.

The depth of investigation of the DITE depends on the resistivity of the rock and on the resistivity contrast between the zone invaded by

drilling fluid and the uninvaded zone. In formations with resistivity higher than 100 Ωm , the average radial depth of investigation of the DITE is about 1.5 m for the deep resistivity phasor induction, 76 cm for the medium resistivity phasor induction, and 38 cm for the shallow spherically focused resistivity. These values drop by about 20% for a 0.1- Ωm formation resistivity.

The DITE also measures spontaneous potential (SP) fields. Spontaneous potentials can originate from a variety of causes: electrochemical, electrothermal, electrokinetic streaming potentials, and membrane potentials due to differences in the mobility of ions in the pore and drilling fluids. The interpretation of SP logs remains problematic due to this multiplicity of sources.

Temperature, Acceleration, and Pressure

Downhole temperature, acceleration, and pressure were measured with the LDEO-TAP tool. When attached to the bottom of the triple combo string, the LDEO-TAP is run in an autonomous mode, with data stored in built-in memory. Two thermistors are mounted near the bottom of the tool to detect borehole fluid temperatures at different rates. A thin fast-response thermistor is able to detect small abrupt changes in temperature. A thicker slow-response thermistor is used to estimate temperature gradients and thermal regimes more accurately. The pressure transducer is included to activate the tool at a specified depth. A three-axis accelerometer measures tool movement downhole, providing data for analyzing the effects of heave on a deployed tool string, which should eventually lead to the fine tuning of the wireline heave compensator (WHC).

The borehole temperature record provides information on the thermal regime of the surrounding formation. The vertical heat flow can be estimated from the vertical temperature gradient combined with measurements of the thermal conductivity from core samples.

The temperature record must be interpreted with caution, as the amount of time elapsed between the end of drilling and the logging operation is generally not sufficient to allow the borehole to recover thermally from the influence of drilling fluid circulations. The data recorded under such circumstances may differ significantly from the thermal equilibrium of that environment. Nevertheless, from the spatial temperature gradient it is possible to identify abrupt temperature changes that may represent localized fluid flow into the borehole, indicative of fluid pathways and fracturing and/or breaks in the temperature gradient that may correspond to contrasts in permeability at lithological boundaries.

Acoustic Velocity

The LSS was used to measure elastic compressional wave velocity in the formation. The LSS provides long spacing measurements through the "depth-derived" borehole compensation principle. Acoustic travel-time readings between two sources and two receivers are memorized at one depth and combined with a second set of readings made after the sonde has been pulled the appropriate distance along the borehole. The LSS records the full waveform for each source-receiver pair, in addition to its automatic determination of arrival time. The depth of investigation for sonic tools depends on the spacing of the detectors and on the

petrophysical characteristics of the rock, such as rock type, porosity, and alteration, but is of the order of tens of centimeters.

The DSI tool employs a combination of monopole and dipole transducers to make accurate measurements of sonic wave propagation in a wide variety of lithologies (Schlumberger, 1994). In addition to a robust and high-quality measurement of compressional wave velocity, the DSI excites a flexural mode in the borehole that can be used to determine shear-wave velocity in all types of formations. When the formation shear velocity is less than the borehole fluid velocity, particularly in unconsolidated sediments, the flexural wave travels at the shear-wave velocity and is the most reliable way to estimate a shear velocity log. The configuration of the DSI also allows recording of cross-line dipole waveforms. These modes can be used to estimate shear-wave splitting caused by preferred mineral and/or structural orientation in consolidated formations. A low-frequency source enables Stoneley waveforms to be acquired as well. The tool configuration and data processing are described in the Leg 174B *Initial Reports* volume (Shipboard Scientific Party, 1998).

Formation MicroScanner

The FMS provides high-resolution, electrical resistivity-based images of borehole walls. The tool has four orthogonal arms (pads); each pad is 50 mm wide and contains 16 microelectrodes, or "buttons," which are pressed against the borehole wall during the recording. The electrodes are arranged in two diagonally offset rows of eight electrodes each and are spaced about 2.5 mm apart. A focused current is emitted from the four pads into the formation, with a return electrode near the top of the tool. Array buttons on each of the pads measure the current intensity variations. Processing transforms these measurements of the microresistivity variations of the formation into continuous, spatially oriented, and high-resolution images that mimic geologic structures behind the borehole walls. Further processing can provide measurements of dip and direction (azimuth) of planar features in the formation. FMS images are particularly useful for mapping structural features, dip determination, detailed core-log correlation, positioning of core sections with poor recovery, and analysis of depositional environments.

The FMS image is sensitive to structures within about 25 cm beyond the borehole wall and has a maximum vertical resolution of 5 mm with a coverage of 25% of the borehole wall for a borehole diameter of 9 7/8 in (i.e., RCB bit size). FMS logging commonly includes two passes, the images of which are merged to improve the borehole-wall coverage. To produce reliable FMS images, however, the pads must be firmly pressed against the borehole wall. The maximum extension of the caliper arms is 15 in. In holes with a diameter larger than 15 in, the pad contact will be inconsistent and the FMS images can be blurred. The maximum borehole deviation where good data can be recorded with this tool is 10°. Irregular borehole walls will also adversely affect the images because contact with the wall is poor.

Borehole Televiewer

The Schlumberger digital BHTV recorded ultrasonic acoustic images during Leg 186. A transducer emits 256 ultrasonic pulses at a frequency of 400 kHz each rotation; these pulses are reflected off the borehole wall and then received by the same transducer. The amplitude and travel-time of the reflected signal are determined and stored in the Schlum-

berger MAXIS computer. A continuous rotation of the transducer and the upward motion of the tool produce a coverage of 100% of the borehole wall.

The amplitude depends on the reflection coefficient of the borehole fluid/rock interface, the position of the BHTV in the borehole, the shape of the borehole, and the roughness of the borehole wall. To decrease the eccentric motions of the tool, a centralizer was mounted immediately above the head of the BHTV and above the NGT (Fig. F8; Table T7). Unfortunately, the design of the BHTV does not allow mounting of a centralizer below the DHTV; thus, eccentric motion of the tool could not be completely eliminated. The change of the borehole wall's roughness (e.g., at fractures intersecting the borehole or in washed-out sections) is responsible for the modulation of the reflected signal; therefore, fractures or changes in character of the drilled rocks can easily be recognized in the amplitude image. On the other hand, the recorded traveltime image gives detailed information about the shape of the borehole, which allows calculation of one caliper value of the borehole from each recorded traveltime (in total, 256 readings per rotation).

Amplitude and traveltime are recorded together with a reference to magnetic north by means of a magnetometer, permitting orientation of images. If features (e.g., fractures) recognized in the core are observed in the BHTV images, orientation of the core is possible. The BHTV can also be used to measure stress in the borehole through identification of borehole breakouts and slip along fault surfaces penetrated by the borehole. In an isotropic, linearly elastic rock subjected to an anisotropic stress field, breakouts take place in the direction of the axis of minimum principal horizontal stress for subvertical boreholes.

Magnetic Field Measurement

Downhole magnetic field measurements were made with the GPIT. The primary purpose of this sonde, which incorporates a three-component accelerometer and a three-component magnetometer, is to determine the acceleration and orientation of the FMS/sonic and BHTV tool strings during logging. The acceleration data allow more precise determination of log depths than is possible on the basis of cable length alone, as the wireline is subject to both stretching and ship heave. Acceleration data are also used in processing of FMS and BHTV data to correct the images for irregular tool motion.

Log Data Quality

The quality of log data may be seriously degraded by excessively wide sections of the borehole or by rapid changes in the hole diameter. Resistivity and velocity measurements are the least sensitive to borehole effects, whereas the nuclear measurements (density, neutron porosity, and both natural and induced spectral gamma rays), FMS, and BHTV are more sensitive because of the large attenuation by borehole fluid or because of poor pad contact. Corrections can be applied to the original nuclear data to reduce the effects of these conditions and, generally, any departure from the conditions under which the tool was calibrated.

Logs from different tool strings may have depth mismatches, caused by either cable stretch or ship heave during recording. Small errors in depth matching can distort the logging results in zones of rapidly changing lithology. To minimize the effects of ship heave, the hydraulic

T7. Logging tool and measurement acronyms, and units of measurement, p. 51.

WHC adjusts for rig motion during logging operations. Distinctive features recorded by the NGT run on every log tool string provide correlation and relative depth offsets among the logging runs and can be calibrated to distinctive lithologic contacts observed in the core recovery or drilling penetration (e.g., basement contacts). Precise core-log depth matching is difficult in zones where core recovery is low because of the inherent ambiguity of placing the recovered section within the cored interval.

In Situ Temperature Measurements

In situ thermal measurements were made using the APC temperature shoe and the DVTP. Techniques using the APC tool are similar to those used since Leg 137 (Shipboard Scientific Party, 1992) and are described in Fisher and Becker (1993).

The DVTP was deployed for the first time during Leg 164 (Shipboard Scientific Party, 1996). The probe has a nearly cylindrical casing that terminates in a pointed tip. In situ temperatures are logged by two thermistors, one located 1 cm from the tip of the probe and the other 12 cm above the tip. A third thermistor, referred to as the internal thermistor, is located in the electronics package. Thermistor sensitivity is 1 mK in an operating range of -5° to 20°C , and the total operation range is -5° to 100°C . In addition to the thermistors, the probe contains an accelerometer sensitive to 0.98 m/s^2 . Both peak and mean acceleration are recorded by the logger. The accelerometer data are used to track disturbances to the instrument package during the equilibration interval. Detailed techniques are described in the Leg 164 *Initial Reports* volume (Shipboard Scientific Party, 1996).

Synthetic Seismograms

Synthetic seismograms can be generated using known density-depth and velocity-depth profiles, the product of which is called acoustic impedance. The impedance in soft sediments is lower, resulting from a lower density and velocity than found in stiffer formations. Any impedance difference between two formations, usually called impedance contrast, could cause a possible seismic reflection. However, the strength and form of a reflection event observed on a field seismic record depends upon the distance of the reflector from the seismic source and the frequency content, in addition to many other factors. Nevertheless, comparison of a synthetic seismogram with a field seismic record are instructive to determine which seismic reflections observed on the record were generated by the drilled strata or geological boundaries.

REFERENCES

- Akiba, F., 1986. Middle Miocene to Quaternary diatom biostratigraphy in the Nankai trough and Japan trench, and modified lower Miocene through Quaternary diatom zones for middle-to-high latitudes of the North Pacific. In Kagami, H., Karig, D.E., Coulbourn, W.T., et al., *Init. Repts. DSDP*, 87: Washington (U.S. Govt. Printing Office), 393–481.
- ASTM, 1989. *Annual Book of ASTM Standards for Soil and Rock: Building Stones* (Vol. 4.08): *Geotextiles*: Philadelphia (Am. Soc. Testing and Mater.).
- Backman, J., and Raffi, I., 1997. Calibration of Miocene nannofossil events to orbitally tuned cyclostratigraphies from Ceara Rise. In Shackleton, N.J., Curry, W.B., Richter, C., and Bralower, T.J. (Eds.), *Proc. ODP, Sci. Results*, 154: College Station, TX (Ocean Drilling Program), 83–99.
- Backman, J., Schneider, D.A., Rio, D., and Okada, H., 1990. Neogene low-latitude magnetostratigraphy from Site 710 and revised age estimates of Miocene nannofossil datum events. In Duncan, R.A., Backman, J., Peterson, L.C., et al., *Proc. ODP, Sci. Results*, 115: College Station, TX (Ocean Drilling Program), 271–276.
- Backman, J., and Shackleton, N.J., 1983. Quantitative biochronology of Pliocene and early Pleistocene calcareous nannofossils from the Atlantic, Indian and Pacific oceans. *Mar. Micropaleontol.*, 8:141–170.
- Baldauf, J.G., and Barron, J.A., 1991. Diatom biostratigraphy: Kerguelen Plateau and Prydz Bay regions of the Southern Ocean. In Barron, J., Larsen, B., et al., *Proc. ODP, Sci. Results*, 119: College Station, TX (Ocean Drilling Program), 547–598.
- Barron, J.A., 1980. Lower Miocene to Quaternary diatom biostratigraphy of Leg 57, off Northeastern Japan, Deep Sea Drilling Project. In von Huene, R., Nasu, N., et al., *Init. Repts. DSDP*, 56, 57 (Pt. 2): Washington (U.S. Govt. Printing Office), 641–685.
- , 1992. Neogene diatom datum levels in the equatorial and North Pacific. In Ishizaki, K., and Saito, T. (Eds.), *The Centenary of Japanese Micropaleontology*: Tokyo (Terra Sci. Publ.), 413–425.
- Barron, J.A., and Gladenkov, A.Y., 1995. Early Miocene to Pleistocene diatom stratigraphy of Leg 145. In Rea, D.K., Basov, I.A., Scholl, D.W., and Allan, J.F. (Eds.), *Proc. ODP, Sci. Results*, 145: College Station, TX (Ocean Drilling Program), 3–19.
- Berger, W.H., Yasuda, M.K., Bickert, T., Wefer, G., and Takayama, T., 1994. Quaternary time scale for the Ontong Java Plateau: Milankovitch template for Ocean Drilling Program Site 806. *Geology*, 22:463–467.
- Berggren, W.A., Kent, D.V., Swisher, C.C., III, and Aubry, M.-P., 1995. A revised Cenozoic geochronology and chronostratigraphy. In Berggren, W.A., Kent, D.V., Aubry, M.-P., and Hardenbol, J. (Eds.), *Geochronology, Time Scales and Global Stratigraphic Correlation*. Spec. Publ.—Soc. Econ. Paleontol. Mineral. (Soc. Sediment. Geol.), 54:129–212.
- Blum, P., 1997. Physical Properties Handbook: a Guide to the Shipboard Measurements of Physical Properties of Deep-sea Cores. *ODP Tech. Note*, 26.
- Boyce, R.E., 1976. Definitions and laboratory techniques of compressional sound velocity parameters and wet-water content, wet-bulk density, and porosity parameters by gravimetric and gamma-ray attenuation techniques. In Schlanger, S.O., Jackson, E.D., et al., *Init. Repts. DSDP*, 33: Washington (U.S. Govt. Printing Office), 931–958.
- , 1977. Deep Sea Drilling Project procedures for shear strength measurement of clayey sediment using modified Wykeham Farrance laboratory vane apparatus. In Barker, P.F., Dalziel, I.W.D., et al., *Init. Repts. DSDP*, 36: Washington (U.S. Govt. Printing Office), 1059–1068.
- Bukry, D., 1973. Low-latitude coccolith biostratigraphic zonation. In Edgar, N.T., Saunders, J.B., et al., *Init. Repts. DSDP*, 15: Washington (U.S. Govt. Printing Office), 685–703.

- , 1975. Coccolith and silicoflagellate stratigraphy, northwestern Pacific Ocean, Deep Sea Drilling Project Leg 32. *In* Larson, R.L., Moberly, R., et al., *Init. Repts. DSDP*, 32: Washington (U.S. Govt. Printing Office), 677–701.
- Cande, S.C., and Kent, D.V., 1995. Revised calibration of the geomagnetic polarity timescale for the Late Cretaceous and Cenozoic. *J. Geophys. Res.*, 100:6093–6095.
- Carlson, R.L., and Christensen, N.I., 1977. Velocity anisotropy and physical properties of deep-sea sediments from the western South Atlantic. *In* Supko, P.R., Perch-Nielsen, K., et al., *Init. Repts. DSDP*, 39: Washington (U.S. Govt. Printing Office), 555–559.
- Ellis, D.V., 1987. *Well Logging for Earth Scientists*: New York (Elsevier).
- Emeis, K.-C., and Kvenvolden, K.A., 1986. Shipboard organic geochemistry on *JOIDES Resolution*. *ODP Tech. Note*, 7.
- Fisher, A., and Becker, K., 1993. A guide to ODP tools for downhole measurements. *ODP Tech. Note*, 10.
- Gealy, E.L., Winterer, E.L., and Moberly, R., Jr., 1971. Methods, conventions, and general observations. *In* Winterer, E.L., Riedel, W.R., et al., *Init. Repts. DSDP*, 7 (Pt. 1): Washington (U.S. Govt. Printing Office), 9–26.
- Gersonde, R., and Burckle, L.H., 1990. Neogene diatom biostratigraphy of ODP Leg 113, Weddell Sea (Antarctic Ocean). *In* Barker, P.F., Kennett, J.P., et al., *Proc. ODP, Sci. Results*, 113: College Station, TX (Ocean Drilling Program), 761–789.
- Gieskes, J.M., Gamo, T., and Brumsack, H., 1991. Chemical methods for interstitial water analysis aboard *JOIDES Resolution*. *ODP Tech. Note*, 15.
- Goldberg, D., 1997. The role of downhole measurements in marine geology and geophysics. *Rev. Geophys.*, 35:315–342.
- Hoppie, B.W., Blum, P., and the Shipboard Scientific Party, 1994. Natural gamma-ray measurements on ODP cores: introduction to procedures with examples from Leg 150. *In* Mountain, G.S., Miller, K.G., Blum, P., et al., *Proc. ODP, Init. Repts.*, 150: College Station, TX (Ocean Drilling Program), 51–59.
- JOIDES Journal, 1992. Ocean Drilling Program guidelines for pollution prevention and safety. *JOIDES J.*, 18.
- Kameo, K., Sato, T., and Takayama, T., 1995. Late Pliocene calcareous nannofossil datums and biohorizons. *In* Flores, J.A., and Sierro, F.J., *Proc. 5th Conf. Int. Nannoplankton Assoc.*, 1993: Salamanca (Univ. de Salamanca), 87–98.
- Koizumi, I., 1985. Diatom biostratigraphy for the Late Cenozoic northwest Pacific. *J. Geol. Soc. Jpn.*, 91:195–211.
- , 1992. Diatom biostratigraphy of the Japan Sea: Leg 127. *In* Pisciotto, K.A., Ingle, J.C., Jr., von Breyman, M.T., Barron, J., et al., *Proc. ODP, Sci. Results*, 127/128 (Pt. 1): College Station, TX (Ocean Drilling Program), 249–289.
- Koizumi, I., and Tanimura, Y., 1985. Neogene diatom biostratigraphy of the middle latitude western North Pacific, Deep Sea Drilling Project Leg 86. *In* Heath, G.R., Burckle, L.H., et al., *Init. Repts. DSDP*, 86: Washington (U.S. Govt. Printing Office), 269–300.
- Kvenvolden, K.A., and McDonald, T.J., 1986. Organic geochemistry on the *JOIDES Resolution*—an assay. *ODP Tech. Note*, 6.
- Lamont-Doherty Earth Observatory-Borehole Research Group, 1994. *Wireline Logging Services Guide*: Lamont-Doherty Earth Observatory-Borehole Research Group.
- Lovell, M.A., Harvey, P.K., Brewer, T.S., Williams, C., Jackson, P.D., and Williamson, G., 1998. Application of FMS images in the Ocean Drilling Program: an overview. *In* Cramp, A., MacLeod, C.J., Lee, S.V., and Jones, E.J.W. (Eds.), *Geological Evolution of Ocean Basins: Results from the Ocean Drilling Program*. Geol. Soc. Spec. Publ. London, 131:287–303.
- Martini, E., 1971. Standard Tertiary and Quaternary calcareous nannoplankton zonation. *In* Farinacci, A. (Ed.), *Proc. 2nd Int. Conf. Planktonic Microfossils Roma*: Rome (Ed. Tecnosci.), 2:739–785.
- Martini, E., and Müller, C., 1986. Current Tertiary and Quaternary calcareous nannoplankton stratigraphy and correlations. *Newsl. Stratigr.*, 16:99–112.

- Mazzullo, J.M., Meyer, A., and Kidd, R.B., 1988. New sediment classification scheme for the Ocean Drilling Program. *In* Mazzullo, J., and Graham, A.G. (Eds.), *Handbook for Shipboard Sedimentologists*. ODP Tech. Note, 8:45–67.
- Motoyama, I., and Maruyama, T., 1998. Neogene diatom and radiolarian biochronology for the middle-to-high latitudes of the Northwest Pacific region: calibration to the Kent's geomagnetic polarity time scales (CK 92 and CK 95). *J. Geol. Soc. Jpn.*, 104:171–183. (in Japanese with English abstract)
- Niitsuma, N., and Koyama, M., 1994. Paleomagnetic processor: a fully automatic portable spinner magnetometer combined with an AF demagnetizer and magnetic susceptibility anisotropy meter. *Shizuoka Univ. Geosci. Rep.*, 21:11–19.
- Ocean Drilling Program, 1996. *Tech Help: a Reference for the Physical Properties Specialist*, Science Services Department, 170.
- Okada, H., and Bukry, D., 1980. Supplementary modification and introduction of code numbers to the low-latitude coccolith biostratigraphic zonation (Bukry, 1973; 1975). *Mar. Micropaleontol.*, 5:321–325.
- Raffi, I., and Flores, J.-A., 1995. Pleistocene through Miocene calcareous nannofossils from eastern equatorial Pacific Ocean. *In* Pisias, N.G., Mayer, L.A., Janecek, T.R., Palmer-Julson, A., and van Andel, T.H. (Eds.), *Proc. ODP, Sci. Results*, 138: College Station, TX (Ocean Drilling Program), 233–286.
- Rider, M., 1996. *The Geological Interpretation of Well Logs* (2nd ed.): Caithness (Whittles Publishing).
- Sato, T., Kameo, K., and Takayama, T., 1991. Coccolith biostratigraphy of the Arabian Sea. *In* Prell, W.L., Niitsuma, N., et al., *Proc. ODP, Sci. Results*, 117: College Station, TX (Ocean Drilling Program), 37–54.
- Schlumberger, 1989. *Log Interpretation Principles/Applications*: Houston, TX (Schlumberger Educ. Services).
- , 1994. *IPL Integrated Porosity Lithology* (Schlumberger Wireline and Testing), SMP-9270.
- Serra, O., 1984. *Fundamentals of Well-Log Interpretation* (Vol. 1): *The Acquisition of Logging Data*: Dev. Pet. Sci., 15A: Amsterdam (Elsevier).
- , 1986. *Fundamentals of Well-Log Interpretation* (Vol. 2): *The Interpretation of Logging Data*. Dev. Pet. Sci., 15B.
- , 1989. *Formation MicroScanner Image Interpretation*: Houston (Schlumberger Educ. Services), SMP-7028.
- Shepard, F., 1954. Nomenclature based on sand-silt-clay ratios. *J. Sediment. Petrol.*, 24:151–158.
- Shipboard Scientific Party, 1992. Introduction and explanatory notes. *In* Becker, K., Foss, G., et al., *Proc. ODP, Init. Repts.*, 137: College Station, TX (Ocean Drilling Program), 5–12.
- , 1995. Explanatory notes. *In* Shipley, T.H., Ogawa, Y., Blum, P., et al., *Proc. ODP, Init. Repts.*, 156: College Station, TX (Ocean Drilling Program), 39–68.
- , 1996. Explanatory notes. *In* Paull, C.K., Matsumoto, R., Wallace, P.J., et al., *Proc. ODP, Init. Repts.*, 164: College Station, TX (Ocean Drilling Program), 13–41.
- , 1998. Introduction. *In* Becker, K., Malone, M.J., et al., *Proc. ODP, Init. Repts.*, 174B: College Station, TX (Ocean Drilling Program), 3–9.
- Stein, R., Brass, G., Graham, D., Pimmel, A., and the Shipboard Scientific Party, 1995. Hydrocarbon measurements at Arctic Gateways sites (ODP Leg 151). *In* Myhre, A.M., Thiede, J., Firth, J.V., et al., *Proc. ODP, Init. Repts.*, 151: College Station, TX (Ocean Drilling Program), 385–395.
- Takayama, T., 1993. Notes on Neogene calcareous nannofossil biostratigraphy of the Ontong Java Plateau and size variations of *Reticulofenestra* coccoliths. *In* Berger, W.H., Kroenke, L.W., Mayer, L.A., et al., *Proc. ODP, Sci. Results*, 130: College Station, TX (Ocean Drilling Program), 179–229.
- Takayama, T., and Sato, T., 1987. Coccolith biostratigraphy of the North Atlantic Ocean, Deep Sea Drilling Project Leg 94. *In* Ruddiman, W.F., Kidd, R.B., Thomas, E.,

- et al., *Init. Repts. DSDP*, 94 (Pt. 2): Washington (U.S. Govt. Printing Office), 651–702.
- Thierstein, H.R., Geitzenauer, K., Molino, B., and Shackleton, N.J., 1977. Global synchronicity of late Quaternary coccolith datum levels: validation by oxygen isotopes. *Geology*, 5:400–404.
- Von Herzen, R.P., and Maxwell, A.E., 1959. The measurement of thermal conductivity of deep-sea sediments by a needle-probe method. *J. Geophys. Res.*, 64:1557–1563.
- Wei, W., 1993. Calibration of Upper Pliocene-Lower Pleistocene nannofossil events with oxygen isotope stratigraphy. *Paleoceanography*, 8:85–99.
- Wentworth, C.K., 1922. A scale of grade and class terms of clastic sediments. *J. Geol.*, 30:377–392.
- Yanagisawa, Y., and Akiba, F., 1998. Refined Neogene diatom biostratigraphy for the northwest Pacific around Japan, with an introduction of code numbers for selected diatom biohorizons. *J. Geol. Soc. Jpn.*, 104:395–414.

Figure F1. Schematic diagram illustrating the ODP labeling scheme used for holes, cores, sections, and samples. IW = interstitial water.

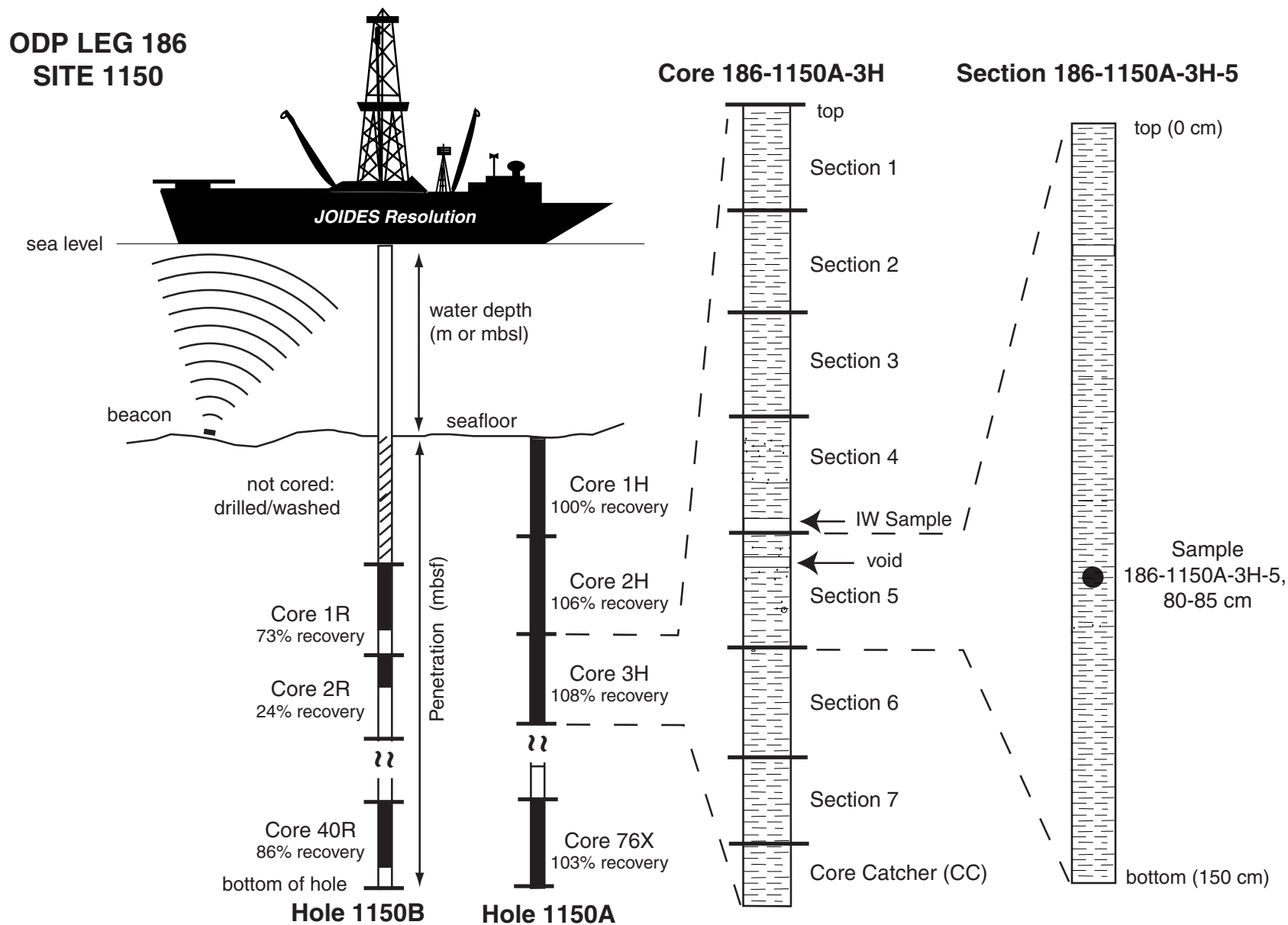





Figure F2. Core description legend for all sites from Leg 186. A. Lithology. (Continued on next two pages.)

LEGEND



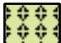




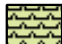
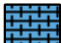

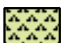



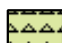


A

Lithology









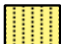



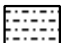



Legend of Major Lithology
for Graphic Lithology column
in core description sheets.

-  Biogenic Components
-  Siliclastic Components
-  Volcaniclastic Components

Pelagic Sediment

- | | | | |
|-------------------------------------------------------------------------------------------------------|------------------------------------------------------------------------------------------------------|----------------------------------------------------------------------------------------------------|--------------------------------------------------------------------------------------------------|
|  Pelagic Limestone |  Nannofossil Ooze |  Diatom-Rad. Ooze |  Diatomite |
|  Foraminiferal Chalk |  Foraminiferal Ooze |  Diatom Ooze |  Radiolarite |
|  Nanno.-Foram. Chalk |  Nanno.-Foram. Ooze |  Radiolarian Ooze |  Spiculite |
|  Calcareous Chalk |  Calcareous Ooze | |  Porcellanite |
|  Nannofossil Chalk | | |  Chert |

Siliciclastic Sediments

- | | | | |
|-------------------------------------------------------------------------------------------------------|------------------------------------------------------------------------------------------------------------------|-------------------------------------------------------------------------------------------------------|-----------------------------------------------------------------------------------------------------|
|  Sand or Sandstone |  Silt or Siltstone |  Clay or Claystone |  Breccia |
|  Silty Sand |  Sandy Silt |  Shale (fissile) |  Gravel |
|  Clayey Sand |  Clayey Silt |  Silty Clay |  Conglomerate |
|  Sand-Silt-Clay |  Siliceous Clay/
Claystone |  Sandy Clay |  Coal and Peat |

Volcaniclastic Sediments





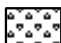

- | | |
|----------------------------------------------------------------------------------------------------------|------------------------------------------------------------------------------------------------------------|
|  Volcanic Ash or Tuff |  Volcaniclastic Sand |
|  Volcanic Lapilli |  Volcaniclastic Breccia |
|  Volcanic Breccia |  Volcaniclastic Silt |

Figure F2 (continued). B. Contacts, sedimentary structures, deformational structure, core disturbance, and bioturbation.

B

Contacts

Sharp	Scoured	Bioturbated	Uncertain
Undulating	Faulted	Inclined	Stylolite
Firmground	Hardground		

Sedimentary Structures

Climbing Ripple	High Angle Tabular Bedding	Planar Lamination
Cross Lamination	Hummocky Cross-stratification	Planar Tabular Bedding
Current Ripple	Imbrication	Reactivation Surface
Flaser Bedding	Low Angle Tabular Bedding	Trough Cross-stratification
Herringbone Cross-strat.	Oscillatory Ripple	Wavy Parallel Bedding
Chaotic Bedding	Graded Bedding	Reverse-Graded Bedding
Convolute Bedding	Lenticular Bedding	Slump
Coarsening Upward	Fining Upward	Cone in Cone Structure
Birdseye Structure, Keystone Vug	Mud Cracks	Tight Zone
Double Mud Drapes	Synaeresis Cracks	

Deformational Structures

Fracture or Fault (displacement visible, but sense not)	Reverse Fault
Joint (no displacement)	Normal Fault
Conjugate Set of Faults	Artificial Fracture (open fracture)

Core Disturbance

Slightly Disturbed	Biscuit	Slightly Fractured
Moderately Disturbed	Gas Expansion	Moderately Fractured
Very Disturbed		Highly Fragmented
Soupy		Breccia






Bioturbation

Common	Moderate	Rare	Barren
--------	----------	------	--------

Figure F2 (continued). C. Fossils and ichnofossils. D. Lithologic accessories.

C

Fossils

- | | | |
|-----------------------------------------------------------------------------------------------------|----------------------------------------------------------------------------------------------------|----------------------------------------------------------------------------------------------------|
|  - Fish Remain |  - Shell Fragment |  - Plant Remain |
|  - Fossil Fragment |  - Spicule | |

Ichnofossils

- | | |
|------------------------------------------------------------------------------------------------------|--------------------------------------------------------------------------------------------------|
|  - Undefined Burrow |  - Zoophycos |
|  - Thalassinoides |  - Chondrites |
|  - Planolites | |

D

Lithologic Accessories

- | | |
|----------------------------------------------------------------------------------------------------------|----------------------------------------------------------------------------------------------------------------|
|  - Ash Layer |  - Silt Lamina |
|  - Coal Lamina |  - Sand Lamina |
|  - Organic Shale Lamina |  - Pebbles/Granules |
|  - Shale Lamina |  - Pebbles/Granules/Sand |
| Wd - Wood Fragments |  - Sand/Silt Patch |
| Py - Pyrite |  - Mottled |
| Gl - Glauconite |  - Ash Patch |
|  - Lithoclast |  - Unknown Patch |
|  - Pumice |  - Sand/Silt Accumulation |
|  - Calcite Concretion | |
|  - Nodule Concretion | |

Figure F3. Leg 186 sediment classification scheme.

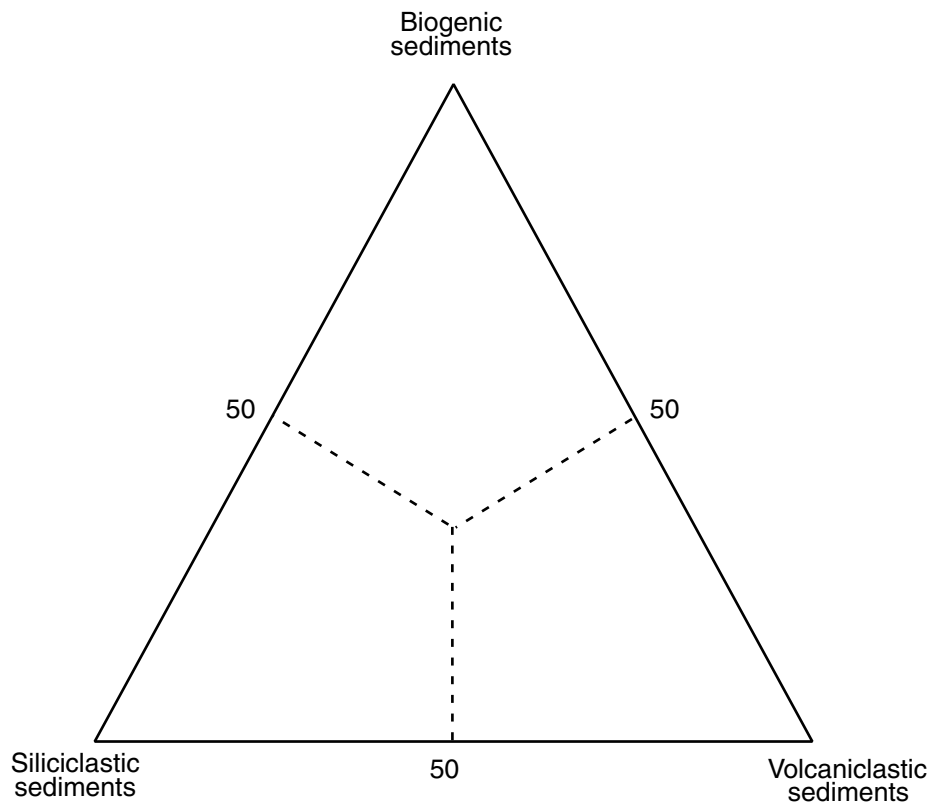


Figure F4. Udden-Wentworth grain-size classification of terrigenous sediments (from Wentworth, 1922).

Millimeters (mm)	Micrometers (μm)	Phi (f)	Udden-Wentworth size class
4096		-12.0	Boulder
256		-8.0	Cobble
64		-6.0	Pebble
4		-2.0	Granule
2.00		-1.0	Very coarse sand
1.00		0.0	Coarse sand
1/2	500	1.0	Medium sand
1/4	250	2.0	Fine sand
1/8	125	3.0	Very fine sand
1/16	63	4.0	Coarse silt
1/32	31	5.0	Medium silt
1/64	15.6	6.0	Fine silt
1/128	7.8	7.0	Very fine silt
1/256	3.9	8.0	Clay
0.00006	0.06	14.0	

Figure F5. Classification scheme used for siliciclastic sediments and rocks during Leg 186 (after Shepard, 1954).

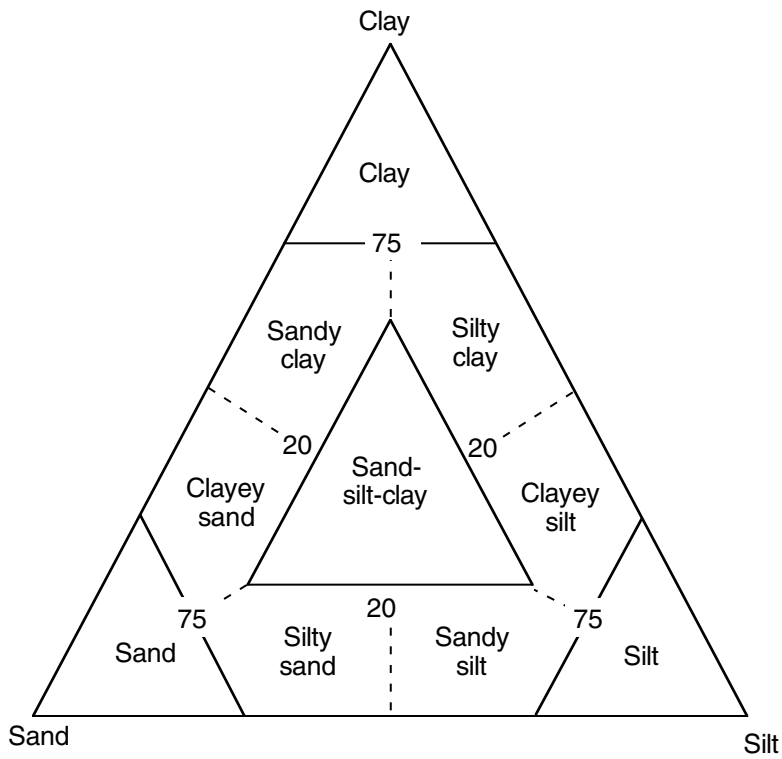


Figure F6. Correlation of the Neogene chronostratigraphy, biostratigraphy, and magnetostratigraphy used during Leg 186. Correlation of the magnetic polarity record and the epoch boundaries follows that of Cande and Kent (1995); diatom biochronology follows Motoyama and Maruyama (1998) and Yanagisawa and Akiba (1998); and nannofossil biochronology follows Berggren et al. (1995). FO = first occurrence; FCO = first common occurrence; LO = last occurrence; and LCO = last common occurrence.

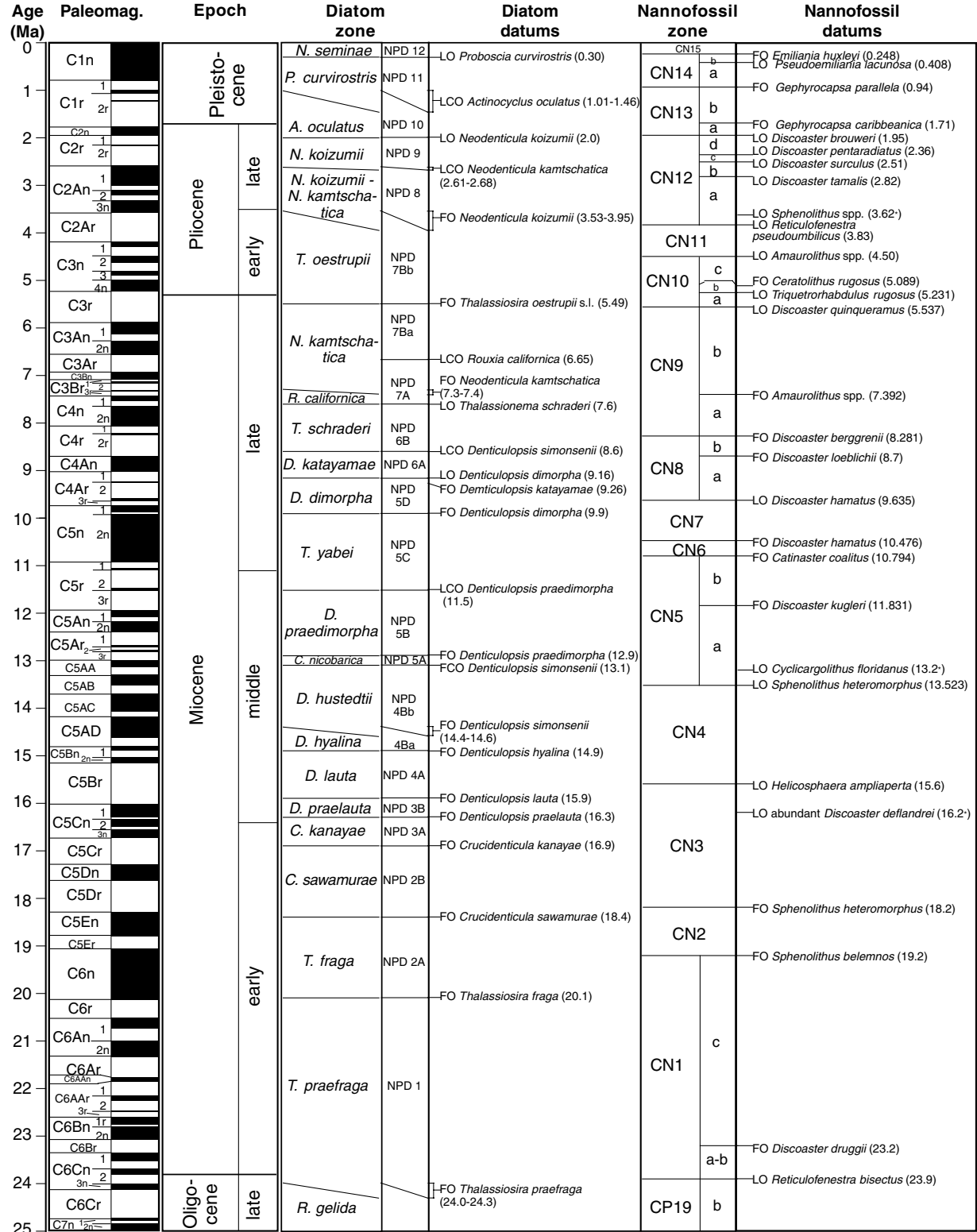


Figure F7. A. ODP paleomagnetic coordinate system for archive and working halves. B. Coordinate system for discrete samples collected with the extruder from the working half. C. Coordinate system for discrete push-in samples.

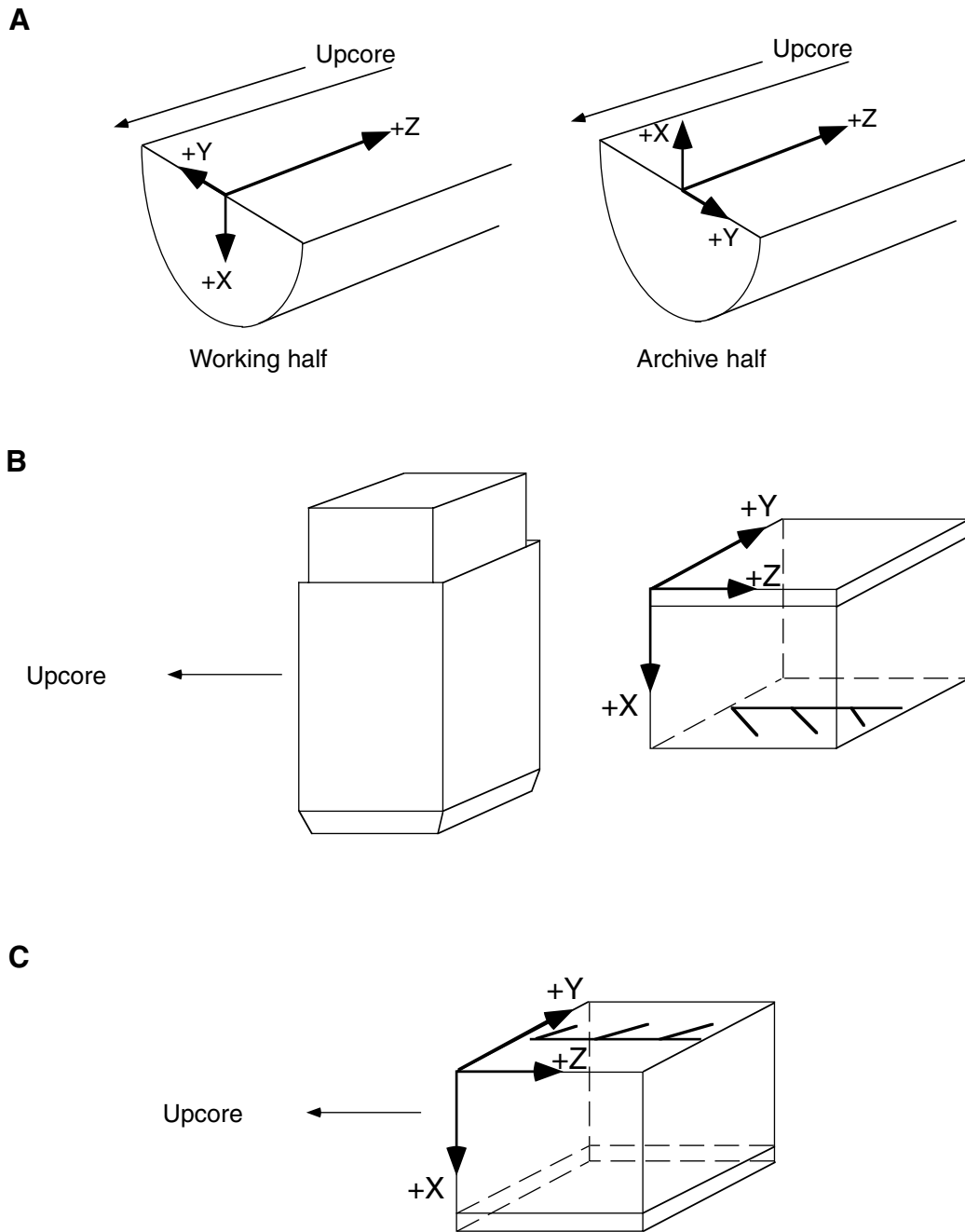


Figure F8. Configuration of tool strings deployed during Leg 186 (not to scale). See Table T7, p. 51, for definitions of logging tool and measurement acronyms.

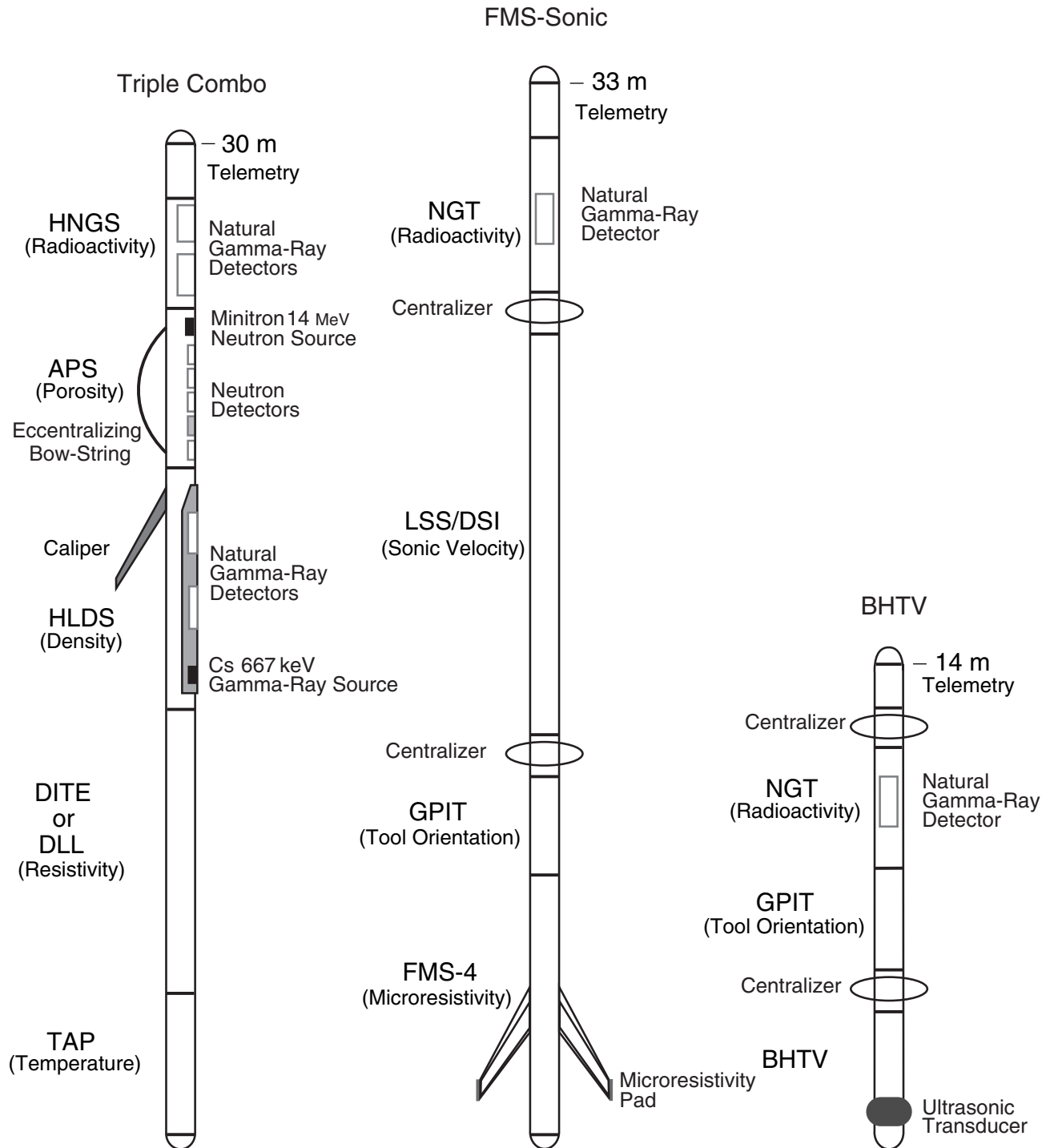


Table T1. X-ray diffraction peaks used for mineral identification.

Minerals	2θ (°)	Peaks (Å)	Intensities
14-Å minerals	6.17-6.25	14.11-14.31	Area
10-Å minerals	8.75-8.93	9.9-10.1	Area
7-Å minerals	12.29-12.65	7.0-7.2	Area
Quartz	20.85	4.26	Peak intensity
Opal-CT	21.94-91.97	4.046-4.051	Area
Opal-A	*	*	Hump
Feldspar	27.71-28.15	3.17-3.20	Peak intensity
Hornblende	28.43	3.14	Peak intensity
Calcite	29.38	3.04	Peak intensity
Clinopyroxene	30.19	2.96	Peak intensity
Dolomite	30.94	2.89	Peak intensity
Halite	31.71	2.82	Peak intensity
Pyrite	33.06	2.71	Peak intensity

Note: *Hump of Opal-A = peak intensities at 21.78° (4.081 Å) – [peak intensities at 16° (5.539 Å) + peak intensities at 39° (2.31 Å)] / 2.

Table T2. Lithologic description of sediments and rocks, including major and minor modifiers.

Sediment class	Principal names	Major modifiers	Minor Modifiers
	>50%, or dominant components when there is no single >50% component	25%-50%	10%-24%
Biogenic (pelagic) grains	<ol style="list-style-type: none"> 1. Ooze 2. Chalk 3. Pelagic limestone 4. Radiolarite 5. Diatomite 6. Spicule 7. Porcellanite 8. Chert 	<ol style="list-style-type: none"> 1. Composition of pelagic grains present in major amounts 2. Texture of siliciclastic grains present in major amounts 3. Composition of all volcaniclasts present in major amounts 	<ol style="list-style-type: none"> 1. Composition of pelagic grains present in minor amounts 2. Texture of siliciclastic grains present in minor amounts 3. Composition of all volcaniclasts present in minor amounts
Siliciclastic grains	<ol style="list-style-type: none"> 1. Gravel 2. Sand 3. Silt 4. Clay, etc. 		
Volcaniclastic grains	<ol style="list-style-type: none"> 1. Breccia 2. Lapilli 3. Ash/tuff 4. Volcanic, etc. 		

Table T3. Estimated ages of diatom events used during Leg 186, based on the time scale of Cande and Kent (1995).

Event	Zone (base)	Age (Ma)	Reference
LO <i>Proboscia curvirostris</i>	NPD12	0.30	1
LO <i>Thalassiosira jouseae</i>		0.30-0.41	2
LO <i>Rhizosolenia matuyamai</i>		0.91-1.06	2
FO <i>Rhizosolenia matuyamai</i>		0.99-1.14	2
LCO <i>Actinocyclus oculatus</i>	NPD11	1.01-1.46	2
LO <i>Stephanopyxis horridus</i>		1.8-2.0	3
LO <i>Thalassiosira antiqua</i>		1.52-1.8	2
FO <i>Fragilariopsis doliolus</i>		2.0	3
LO <i>Neodenticula koizumii</i>	NPD10	2.0	1
LO <i>Pyxidicula pustulata</i>		2.0-2.14	4
LO <i>Thalassiosira convexa</i>		2.35	3
LCO <i>Neodenticula kamtschatica</i>	NPD9	2.61-2.68	2
FO <i>Neodenticula seminae</i>		2.68	1
LO <i>Thalassiosira marujamica</i>		3.08-3.2	5
LO <i>Thalassiosira jacksonii</i>		3.08-3.41	1
LO <i>Neodenticula koizumii</i>	NPD8	3.53-3.95	2
FO <i>Actinocyclus oculatus</i>		3.64-4.01	1
FO <i>Thalassiosira latimarginata</i>		5.07	5
FO <i>Thalassiosira oestrupii</i> s.l.	NPD7Bb	5.49	3
LO <i>Thalassiosira miocenica</i>		6.0	2
FO <i>Thalassiosira praeoestrupii</i>		6.1	5
LCO <i>Rouxia californica</i>	NPD7Ba	6.65	6
LO <i>Cavitatus jouseanus</i>		6.7-6.8	5
FO <i>Nitzschia reinholdii</i>		7.4-7.5	5
FO <i>Neodenticula kamtschatica</i>		7.3-7.4	5
FO <i>Thalassionema schraderi</i>	NPD7A	7.6	5
FO <i>Thalassiosira antiqua</i>		8.5	3
LO <i>Denticulopsis katayamae</i>		8.5	3
LCO <i>Denticulopsis simonsenii</i>	NPD6B	8.6	5
LO <i>Denticulopsis dimorpha</i>	NPD6A	9.16	5
FO <i>Denticulopsis katayamae</i>		9.26	5
FO <i>Thalassionema schraderi</i>		9.5	5
FO <i>Denticulopsis dimorpha</i>	NPD5D	9.9	5
LO <i>Nitzschia heteropolica</i>		10.8-11.0	5
LO <i>Mediaria splendida</i>		10.8-11.0	5
LCO <i>Denticulopsis praedimorpha</i>	NPD5C	11.5	5
FO <i>Proboscia barboi</i>		12.3	5
LO <i>Crucidentricula nicobarica</i>		12.5	3
FO <i>Denticulopsis praedimorpha</i>	NPD5B	12.9	7
FCO <i>Denticulopsis simonsenii</i>	NPD5A	13.1	3
FO <i>Denticulopsis simonsenii</i>	NPD4Bb	14.4-14.6	5
FO <i>Denticulopsis hyalina</i>	NPD4Ba	14.9	5
FO <i>Actinocyclus ingens</i> v. <i>nodus</i>		15.1	3
FO <i>Denticulopsis lauta</i>	NPD4A	15.9	3
FO <i>Denticulopsis praelauta</i>	NPD3B	16.3	3
FO <i>Crucidentricula kanayae</i>	NPD3A	16.9	5
FO <i>Crucidentricula sawamurae</i>	NPD2B	18.4	3
FO <i>Thalassiosira fraga</i>	NPD2A	20.1	8
FO <i>Thalassiosira praefraga</i>	NPD1	24.0-24.3	8

Notes: LO = last occurrence, FO = first occurrence, LCO = last common occurrence, FCO = first common occurrence. References are as follows: 1 = Koizumi (1992); 2 = Koizumi and Tanimura (1985); 3 = Barron (1992); 4 = Barron (1980); 5 = Barron and Gladenkov (1995); 6 = Akiba (1986); 7 = Gersonde and Burckle (1990); 8 = Baldauf and Barron (1991).

Table T4. Estimated ages of calcareous nannofossil events used during Leg 186, based on the time scales of Cande and Kent (1995) and Berggren et al. (1995).

Event	Zone (base)	Age (Ma)	Reference
FO <i>acme Emiliana huxleyi</i>		0.085	1
LO <i>Helicosphaera inversa</i>		0.155	2
FO <i>Emiliana huxleyi</i>	CN15	0.248	2
LO <i>Pseudoemiliana lacunosa</i>	CN14b	0.408	2
FO <i>Helicosphaera inversa</i>		0.505	2
LO <i>Reticulofenestra asanoi</i>		0.88	3
FO <i>Gephyrocapsa parallela</i>	CN14a	0.94	3
FO <i>Reticulofenestra asanoi</i>		1.17	3
LO <i>Helicosphaera sellii</i>		1.26	3
LO <i>Calcidiscus macintyreii</i>		1.64	3
FO <i>Gephyrocapsa oceanica</i>		1.64	3
FO <i>Gephyrocapsa caribbeanica</i>	CN13b	1.71	4
Pliocene/Pleistocene boundary		1.745	2
LO <i>Discoaster brouweri</i>	CN13a	1.95	3
LO <i>Discoaster pentaradiatus</i>	CN12d	2.36	3
LO <i>Discoaster surculus</i>	CN12c	2.51	3
LO <i>Discoaster tamalis</i>	CN12b	2.82	2
LO <i>Sphenolithus</i> spp.	CN12a	3.62	5
LO <i>Reticulofenestra pseudoumbilicus</i>	CN12a	3.83	3
LO <i>Amaurolithus</i> spp.	CN11	4.50	6
FO <i>Ceratolithus rugosus</i>	CN10c	5.046	7
FO <i>Ceratolithus acutus</i>	CN10b	5.089	7
LO <i>Triquetrorhabdulus rugosus</i>		5.231	7
Miocene/Pliocene boundary		5.3	
LO <i>Discoaster quinquerramus</i>	CN10a	5.537	7
LO <i>Amaurolithus amplificus</i>		5.993	7
FO <i>Amaurolithus amplificus</i>		6.840	7
LO <i>paracme R. pseudoumbilicus</i>		7.100	7
FO <i>Amaurolithus</i> spp.	CN9b	7.392	7
FO <i>Discoaster berggrenii</i>	CN9a	8.281	7
FO <i>Discoaster loeblichii</i>	CN8b	8.7	8
FO <i>paracme R. pseudoumbilicus</i>		8.788	7
LO <i>Discoaster hamatus</i>	CN8a	9.635	7
LO <i>Catinaster calyculus</i>		9.641	7
FO <i>Discoaster neohamatus</i>		10.450	7
FO <i>Discoaster hamatus</i>	CN7	10.476	7
FO <i>Catinaster calyculus</i>		10.705	7
FO <i>Catinaster coalitus</i>	CN6	10.794	7
LO <i>Coccolithus miopelagicus</i>		10.941	7
LO <i>Discoaster kugleri</i>		11.520	7
FO <i>Discoaster kugleri</i>	CN5b	11.831	7
LO <i>Cyclicargolithus floridanus</i>		13.2	9
LO <i>Sphenolithus heteromorphus</i>	CN5a	13.523	7
LO <i>Helicosphaera ampliapertura</i>	CN4	15.6	8
LO abundant <i>Discoaster deflandrei</i>		16.2	9
FO <i>Sphenolithus heteromorphus</i>	CN3	18.2	8
LO <i>Sphenolithus belemnus</i>		18.3	8
FO <i>Sphenolithus belemnus</i>	CN2	19.2	8
FO <i>Discoaster druggii</i>	CN1c	23.3	10
LO <i>Sphenolithus capricornutus</i>		23.7	8
Oligocene/Miocene boundary		23.8	
LO <i>Sphenolithus delphix</i>		23.8	8
LO <i>Reticulofenestra bisecta</i>	CN1a	23.9	8

Notes: FO = first occurrence, LO = last occurrence. References are as follows: 1 = Thierstein et al. (1977); 2 = modified from Takayama and Sato (1987), Sato et al. (1991), Takayama (1993), and Kameo et al. (1995); 3 = Wei (1993); 4 = Berger et al. (1994); 5 = Backman and Schackleton (1983); 6 = Backman et al. (1990); 7 = Backman and Raffi (1997); 8 = Berggren et al. (1995); 9 = Raffi and Flores (1995).

Table T5. Measured and calculated parameters, assumptions, and relationships for index properties calculations.

Parameters and assumptions	Relationships	Unit
Measured parameters		
M_t (wet mass)		g
M_d (dry mass)		g
V_d (dry volume)		cm ³
Assumptions		
S (salinity of pore water)	$S = 0.035$	
ρ_{salt} (density of evaporated salt)	$\rho_{\text{salt}} = 2.20$	g/cm ³
ρ_{pw} (density of pore water)	$\rho_{\text{pw}} = 1.024$	g/cm ³
Calculated parameters		
M_{pw} (mass of pore water)	$M_{\text{pw}} = (M_t - M_d) / (1 - S)$	g
M_s (mass of solids)	$M_s = M_t - M_{\text{pw}}$	g
M_{salt} (mass of salt)	$M_{\text{salt}} = M_{\text{pw}} - M_t + M_d$	g
V_{pw} (volume of pore water)	$V_{\text{pw}} = M_{\text{pw}} / \rho_{\text{pw}}$	cm ³
V_{salt} (volume of salt)	$V_{\text{salt}} = M_{\text{salt}} / \rho_{\text{salt}}$	cm ³
V_s (volume of solids)	$V_s = V_d - V_{\text{salt}}$	cm ³
V_t (total volume)	$V_t = V_s + V_{\text{pw}}$	cm ³
W_t (water content of total mass)	$W_t = 100 \cdot M_{\text{pw}} / M_t$	%
W_s (water content of mass of solids)	$W_s = 100 \cdot M_{\text{pw}} / M_s$	%
ρ_b (bulk density)	$\rho_b = M_t / V_t$	g/cm ³
ρ_d (dry density)	$\rho_d = M_s / V_t$	g/cm ³
ρ_g (grain density)	$\rho_g = M_s / V_s$	g/cm ³
η (porosity)	$\eta = 100 \cdot V_{\text{pw}} / V_t$	%
e (void ratio)	$e = V_{\text{pw}} / V_s$	

Table T6. Leg 186 logging tools and their applications.

Tool string	Typical speed (m/hr)	Tool	Aim of measurements	Sampling interval (cm)	Vertical resolution (cm)
Integrated porosity-lithology tool (IPLT)	250-275	HNGS	Natural gamma radiation	15	45
		APS	Porosity	15	30
		HLDT	Bulk density	15	45
		DITE/SFL	Resistivity	15	75/150/200
		TAP	Temperature/acceleration/pressure	1 per s	NA
Formation MicroScanner (FMS)/sonic	250-275	NGT	Natural gamma radiation	15	45
		DSI/LSS	Sonic velocity	15	60/120
		GPIT	Orientation	0.25	NA
		MEST/FMS	Microresistivity	0.25	3
Borehole televiewer (BHTV)	250-275	NGT	Natural gamma radiation	15	45
		BHTV	Sonic imaging	1	NA

Note: NA = not applicable. See Table T7, p. 51, for definition of acronyms used to describe tool strings and individual tool names.

Table T7. Logging tool and measurement acronyms, and units of measurement.

Tool	Output	Explanation	Units
HNGS		Hostile environment spectral gamma-ray sonde	
	HSGR	Total spectral gamma ray	gAPI
	HCGR	Computed uranium-free gamma ray (HSGR-HURA)	gAPI
	HFK	Formation potassium	wt%
	HTHO	Thorium	ppm
	HURA	Uranium	ppm
APS		Accelerator porosity sonde	
	APSC	Near array porosity (sandstone corrected)	%
	FPSC	Far array porosity (sandstone corrected)	%
	SIGF	Neutron capture cross section of the formation (Sf)	cu
	STOF	Estimated tool standoff (tool distance from borehole wall)	in
HLDS		Hostile environment lithodensity sonde	
	RHOB	Bulk density (corrected)	g/cm ³
	PEF	Photoelectric effect factor	barn/e ⁻
	DRHO	Delta-rho (bulk density correction)	g/cm ³
	CALI	Caliper (measure of borehole diameter)	in
DITE		Dual induction tool	
	IDPH	Phasor induction (deep resistivity)	Ωm
	IMPH	Phasor induction (medium resistivity)	Ωm
	SFLU	Shallow spherically focused resistivity	Ωm
LDEO-TAP		Temperature/acceleration/pressure tool	
	T, A, P	Temperature, acceleration, pressure	°C, mm/s ² , psi
NGT		Natural gamma-ray spectrometry tool	
	SGR	Standard (total) gamma ray	gAPI
	CGR	Corrected gamma ray	gAPI
DSI/LSS		Dipole shear sonic imager or long-spaced sonic imager	
	DT	V _p transit time	μs/ft
GPIT		General purpose inclinometer tool	
	DEVI	Hole deviation	°
	HAZI	Hole azimuth	°
	P1AZ	Pad One azimuth	°
	C1, C2	Orthogonal hole diameters [Caliper 1, Caliper 2 (from FMS tool)]	in
	FCA(X,Y,Z)	Total acceleration vector components	m/s ²
	F(X,Y,Z)	Total magnetic field vector components	oersted
MEST/FMS		Microelectrical resistivity tool or Formation MicroScanner	
		Spatially oriented borehole wall resistivity image	NA